Magnetic Resonance Imaging 55 (2019) 153–170

Contents lists available at ScienceDirect

Magnetic Resonance Imaging

journal homepage: www.elsevier.com/locate/mri

Original contribution

HASAN: Highly accurate sensitivity for auto-contrast-corrected pMRI reconstruction

Md. Sakibur Rahman Sajal, Md. Kamrul Hasan*

Department of Electrical and Electronic Engineering, Bangladesh University of Engineering and Technology (BUET), Dhaka 1000, Bangladesh

ARTICLE INFO

Keywords:
Parallel MRI
Coil-map estimation
SIMO model
Cross-relation error
Constrained multi-channel adaptive algorithm
Auto contrast correction

ABSTRACT

A novel method for highly accurate coil sensitivity-map estimation, based on a constrained image-domain multi-channel LMS (c-iMCLMS) algorithm, is proposed for image reconstruction using self-calibrating SENSE. The sensitivity information is extracted by developing an image-domain cross-relation equation using the low-resolution images constructed from the fully sampled central region of the variable density MR data. Then this formulation is solved in an iterative way using a novel sum-of-squares (SOS) constraint. The improvement of the convergence speed of the c-iMCLMS algorithm is accomplished by SOS normalization of the low resolution image data and using a variable step-size in the update equation. The salient feature of the proposed technique is that it does not require any prior selection of the basis function and/or simultaneous estimation of the object image and the coil sensitivity-map. Only the low resolution images are re-filtered for the compensation of the data truncation effect to improve the consistency of the estimated coil maps. Besides, the application of the novel SOS-constraint, estimated using the pixel position-wise variance of the coil maps, gives closest to the true sensitivity-map. As a result, true object image with auto-corrected contrast is reconstructed without adopting any traditional post-contrast correction techniques. For minimization of the process noise, regularized conjugate gradient (CG) based SENSE reconstruction algorithm is used for image reconstruction using the estimated coil sensitivity-map. The proposed technique is tested on various simulation, synthetic and *in-vivo* datasets and significant signal-to-artifact-noise-ratio (SANR) improvement closest to the theoretical limit set by coil geometric factor is obtained as compared to some noted techniques in the literature both visually and numerically.

1. Introduction

The accelerated MR scan has gained a significant attention in the field of parallel MRI (pMRI) [1] because of the drastic reduction in data acquisition time by under-sampling the *k*-space in the time-consuming phase encode direction at an expense of the resulting aliasing in the image space [2]. For generating a high quality image by negating the aliasing artifact, various reconstruction techniques have been proposed [3] among which GRAPPA and SENSE are the commercially used most popular techniques [4].

GRAPPA subscribes to the philosophy that the forfeited *k*-space lines can be estimated from the central fully sampled auto-calibration-signal (ACS) lines if an accurate fitting can be employed and thereafter summing the squares of the individual coil images gives the sum-of-squares (SOS) reconstructed image [5]. On the other hand, SENSE exploits the inherent sensitivity encoding embedded by the receiver coils in the image space for image reconstruction by employing pseudo matrix inversion on the aliased image space data [6]. The Generalized SENSE (GSENSE) [7] is an improvement of SENSE that uses the conjugate gradient (CG) method [8] for obtaining a better quality reconstructed image compared to the basic SENSE [6] by incorporating regularization [9]. SENSE based techniques can produce optimal quality [10] images provided that the estimates of the coil sensitivity maps or in short the coil maps are accurate [11].

Conventional SENSE based techniques divide individual coil data by the body coil image to produce the coil maps. Body coil image is generally obtained by Walsh [12] or SOS method [10] with the former commonly used under low signal-to-noise-ratio (SNR) condition for its better performance. In some methods, coil map estimation is followed by an optional polynomial smoothing [6]. However because of the inhomogeneity of the magnetic field [13], the body coil image exhibits more or less contrast ambiguity unless properly corrected. Therefore in case of bird-cage RF coils for imaging objects like head [14], conventional methods introduce contrast ambiguity in the center of the

* Corresponding author.
E-mail addresses: sakibsajal017@gmail.com (Md. S.R. Sajal), khasan@eee.buet.ac.bd (Md. K. Hasan).
URL: http://khasan.buet.ac.bd/ (Md. K. Hasan).

https://doi.org/10.1016/j.mri.2018.09.007
Received 2 June 2018; Received in revised form 5 September 2018; Accepted 8 September 2018

reconstructed image [15] and require additional post-contrast correction [16]. For surface coil while imaging object like spine, this contrast problem is sever at the distant end from the coil surface and commonly known as the surface flare [17] which requires similar post processing as well. Moreover, polynomial smoothing of the coil maps *after* coil-map estimation to remove any localized discontinuities results in inconsistency of the estimated coil maps with the acquired coil data. On the other hand, theoretical model based coil-map estimation is also used in [18,19] which additionally requires the knowledge of the location and orientation of the receiver coils. Some methods simply use the information available in the image to generate the coil sensitivity maps [20,21]. All these approaches generate a poor reconstructed image with residual aliasing [2] particularly at higher acceleration factors because of the inaccuracy of the estimated coil maps. Even use of a pre-scan for coil-map estimation is not advantageous because of the change in the patient's or the organs' position during the pre-scan and the following accelerated scan [2]. Therefore, conventional SENSE based methods cannot produce the true coil-maps employing such body coil image and hence fail to reconstruct the true object image directly.

Although GRAPPA does not require any coil maps for reconstruction, still the reconstructed image exhibits contrast ambiguity [22] as the field inhomogeneity is embedded in the coil-data through coil-maps. Therefore, a post-processing is required to correct the contrast of the reconstructed image in case of GRAPPA as well. Besides, the accuracy of the weights to estimate the coil data paradoxically varies with increase of ACS [23] while in case of SENSE, accuracy of the coil maps increases more regularly.

In this paper, we propose a novel method for the estimation of highly accurate coil maps using a new blind technique based on a constrained image-domain multi-channel LMS (c-iMCLMS) algorithm. This self calibrating method minimizes the truncation effect [24] in the low resolution images constructed from ACS before estimation by using a new approach to improve coil-map consistency. Then an image domain cross-relation formulation is developed and solved for coil-map estimation. A novel SOS-constraint based on the coil-map correlation is used to ensure the accuracy of the estimated coil maps. As a result, reconstructed images by employing the proposed coil maps with CG-SENSE algorithm do not require any post-contrast correction as like in the SOS reconstruction [15]. The effect of using highly accurate coil maps contributes in archiving higher signal-to-artifact-ratio (SANR) close to the theoretical limit imposed by the *ideal* coil maps at different outer-reduction-factor (ORF) as observed in different data sets.

2. Theory

2.1. Problem formulation for image reconstruction in pMRI

In pMRI [1], the process of data acquisition can be modeled as a SIMO system [15] since the obtained *k*-space MR data by different coils can be modeled as convolution of the original object image and the respective coil sensitivities.

In spatial domain the inverse Fourier transform of this convoluted coil-data, $\mathbf{X}_\gamma(\mathbf{r}_\rho),\gamma = 1,2,\cdots M$, where M denotes the total number of coils, can be modeled as the pixel position-wise multiplication of the original object image, $\mathbf{X}_0(\mathbf{r}_\rho)$ with the corresponding coil-map, $\mathbf{S}_\gamma(\mathbf{r}_\rho),\gamma = 1,2,\cdots M$, as shown in Fig. 1 and given by the following equation:

$$\mathbf{X}_\gamma(\mathbf{r}_\rho) = \mathbf{X}_o(\mathbf{r}_\rho)\cdot\mathbf{S}_\gamma(\mathbf{r}_\rho),\ \gamma = 1,\ 2,\ \cdots,\ M \tag{1}$$

Here and from this point, '·' will indicate element-wise multiplication between involved matrices/vectors and $\mathbf{r}_\rho$ denotes the index of the ρ-th pixel of the associated full field-of-view (FOV) images, i.e., $\mathbf{X}_\gamma$, $\mathbf{X}_0$, $\mathbf{S}_\gamma$. Since data acquisition is accelerated in pMRI by under-sampling the *k*-space, the resulting aliased image [see Fig. 2 (a1) for ORF = 4] with reduced FOV can be described by the following equation [for details see [3]]:

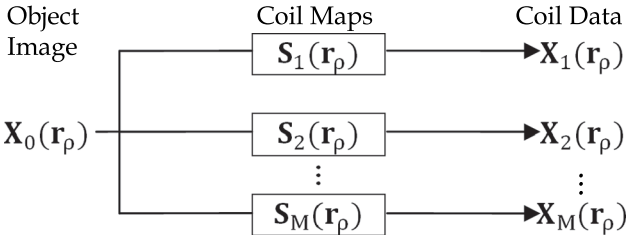

Fig. 1. Data acquisition: The SIMO model for data ($\mathbf{X}_\gamma$) acquisition by multiple receiver coils with different sensitivity profiles ($\mathbf{S}_\gamma$) to image the common object ($\mathbf{X}_0$).

$$\mathbf{I}_\gamma(\mathbf{r}_\rho) = \sum_{\rho=1}^{R}\mathbf{X}_\gamma(\mathbf{r}_\rho) = \sum_{\rho=1}^{R}\mathbf{X}_o(\mathbf{r}_\rho)\cdot\mathbf{S}_\gamma(\mathbf{r}_\rho) \tag{2}$$

Here, $\mathbf{I}_\gamma(\mathbf{r}_\rho)$ represents the aliased pixel in the reduced FOV, coil index $\gamma = 1,2,\cdots,M$ and pixel index $\rho = 1,2,\cdots,R$ specifies the involved pixel locations which have been aliased. Concatenating the aliased pixels of all the coils in the vector $\mathbf{I}$ and the pixels from the associated coil maps in matrix $\mathbf{S}$, we can rewrite Eq. (2) as follows [3]:

$$\mathbf{I} = \mathbf{S}\mathbf{X}_\mathbf{o} \tag{3}$$

The following matrix inversion can be used for the restoration of the *aliasing-free* original object image [see Fig. 2 (a3)] if an *accurate* knowledge of the true coil maps [see Fig. 2 (a2)] is available [3], [6]:

$$\mathbf{X}_\mathbf{o} = (\mathbf{S}^H\mathbf{S})^{-1}\mathbf{S}^H\mathbf{I} \tag{4}$$

At this point, the sources of errors/noise in the reconstructed image have to be specified. First of all, the geometric factor or in short *g*-factor which arises from the ill-conditioning of the inverse matrix in Eq. (4) is given by [6]

$$g(\mathbf{r}_\rho) = \sqrt{[(\mathbf{S}^H\Psi\mathbf{S})^{-1}]_{\rho,\rho}\,[(\mathbf{S}^H\Psi\mathbf{S})]_{\rho,\rho}} \geq 1. \tag{5}$$

Here, Ψ is the noise-correlation matrix among the coils. Unless the true coil maps are ideal ones [3], *g*-factor deteriorates the pixel-position wise varying SNR especially in the location where the coil maps have higher correlation, in other words, close pixel values. With increase of ORF, values of the *g*-factor vary according to coil-correlation. However, the correlation among the coil maps is embedded in the coil data based on coil geometry (from which the name geometric factor comes) and therefore cannot be altered during estimation. Therefore, the *g*-factor map, also known as the *g*-map of the estimated coil maps can be no better than that generated by the true coil maps. Secondly, although Eqs. (3) and (4) imply that the true coil-map pixels comprise $\mathbf{S}$, Eq. (1) does not restrict on *only* one set of possible coil maps that generates identical coil data, $\mathbf{X}_\gamma$. In other words, dividing the true coil maps element-wise with an arbitrary matrix $\mathbf{A}$ [see Fig. 2 (b1)] having all non-zero elements and at the same time multiplying the original image, $\mathbf{X}_\mathbf{o}$ element-wise with the same matrix $\mathbf{A}$ [see Eq. (6)], we get the same coil-data, $\mathbf{X}_\gamma$ as before from a new set of coil maps, $\bar{\mathbf{S}}_\gamma$ [see Fig. 2 (b2)] and object image, $\bar{\mathbf{X}}_\mathbf{o}$.

$$\mathbf{X}_\gamma = \mathbf{X}_o\cdot\mathbf{S}_\gamma = (\mathbf{X}_o\cdot\mathbf{A})\cdot(\mathbf{S}_\gamma.\ /\mathbf{A}) = \bar{\mathbf{X}}_o\cdot\bar{\mathbf{S}}_\gamma \tag{6}$$

Here and from this point ' ./' will represent element-wise division. Therefore, use of $\bar{\mathbf{S}}$ instead of $\mathbf{S}$ in Eq. (4) produces an aliasing-free reconstructed image, $\bar{\mathbf{X}}_o$ [see Fig. 2 (b3)] masked by $\mathbf{A}$. We will call such coil maps as *consistent* coil maps since these are *mathematically* consistent to produce an aliasing-free reconstructed image (however, not the *true* object image). Conventional coil maps, $\mathbf{Cmap}_\gamma$ produced by SOS normalization of the coil data using Eq. (7) are consistent however masked by the true coil-SOS, $\mathbf{SOS}_t = \sqrt{\sum_\gamma|\mathbf{S}_\gamma|^2}$ as:

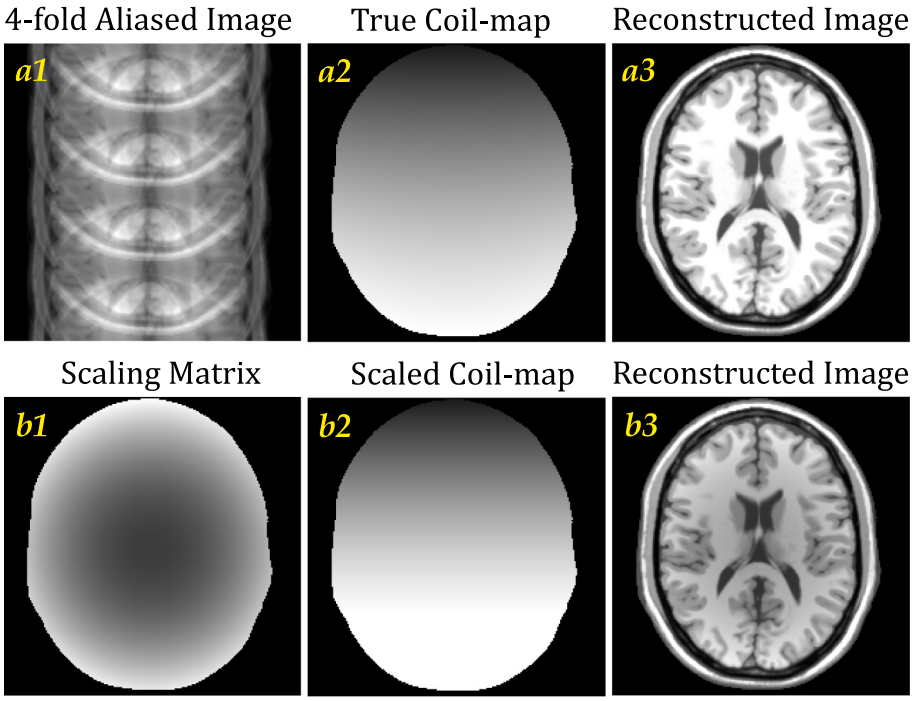

Fig. 2. Aliasing-free reconstruction from consistent coil maps: a1) 4-fold aliased image, a2) 1 of 8 true coil maps, a3) aliasing-free reconstruction, b1) arbitrary matrix, **A**, b2) resulting coil-map (consistent) after division by **A**, and b3) aliasing-free reconstruction (pixel position-wise differently scaled).

$$\mathbf{Cmap}_\gamma = \frac{\mathbf{x}_\gamma}{\sqrt{\sum_\gamma |\mathbf{x}_\gamma|^2}} = \frac{\mathbf{x}_o \times \mathbf{s}_\gamma}{\sqrt{\mathbf{x}_o^2 \times \sum_\gamma |\mathbf{s}_\gamma|^2}} = \mathbf{S}_\gamma ./\mathbf{SOS}_t = \mathbf{S}_\gamma ./\mathbf{A} = \bar{\mathbf{S}}_\gamma,\ \gamma = 1, 2, \cdots, M \tag{7}$$

Here $|\cdot|^2$ represents element-wise square of the absolute values of the associated matrices. Therefore, the associated SOS reconstructed image is also masked by $\mathbf{SOS}_t$ as

$$\mathbf{X}_{SOS} = \overline{\mathbf{X}}_o = \mathbf{X}_o \cdot \mathbf{A} = \mathbf{X}_o \cdot \mathbf{SOS}_t \tag{8}$$

and requires additional post-contrast correction since $\mathbf{SOS}_t$ is non-uniform in practice. This non-uniform coil-SOS is the source of contrast ambiguity in the conventional SOS reconstructed image. However as explained in the following, the proposed method estimates the *accurate* coil maps, $\mathbf{S}_\gamma$ by virtue of the SOS-constraint based on coil-map *correlation* and thereby directly reconstruct the auto-contrast-corrected true object image $\mathbf{X}_o$ without requiring any additional post-contrast correction [25].

Finally, the estimated coil maps lose consistency with the acquired coil data in the cases where basis functions are inaccurately chosen or coil maps are smoothed after estimation. Similar problem is faced when coil maps are estimated from the central lines of variable density MR data in self-calibrating SENSE. The low resolution image violates the relation in Eq. (1) and the estimated coil maps become inconsistent. To address this problem in our proposed method, the low resolution coil data are re-filtered to compensate for the truncation effect using a new iterative approach before coil map estimation. Therefore, coil-map accuracy improves without adopting any post-smoothing or requiring any basis functions for coil maps. This improvement in consistency gives better result at higher acceleration factors compared to other conventional methods.

2.2. Development of a cross-relation formulation

Using Eq. (1), a cross-relation formulation between the i-th and j-th coils, where $i,j = 1,2,\ldots,M, i \neq j$ can be written as

$$\mathbf{x}_i(\rho) \cdot \mathbf{s}_j(\rho) = \mathbf{x}_o(\rho) \cdot \mathbf{s}_i(\rho) \cdot \mathbf{s}_j(\rho) = \mathbf{x}_j(\rho) \cdot \mathbf{s}_i(\rho). \tag{9}$$

Here vectors $\mathbf{x}_o$, $\mathbf{s}_i$ and $\mathbf{x}_i$ represent the object image, i-th coil-map and coil-data, respectively and ρ denotes the $\mathbf{r}_\rho$-th pixel in the 2-D image. Using the estimates, $\hat{\mathbf{s}}_\gamma$ instead of the true coil maps, a cross-relation error vector can be defined as

$$\mathbf{e}_{ij} = \mathbf{D}_{\mathbf{x}_i} \hat{\mathbf{s}}_j - \mathbf{D}_{\mathbf{x}_j} \hat{\mathbf{s}}_i,\ i, j = 1, 2, \cdots, M,\ i \neq j \tag{10}$$

where $\mathbf{D}_{\mathbf{x}_\gamma}$ is a diagonal matrix with $\gamma = 1,2,\cdots,M$ and

$$\mathbf{D}_{\mathbf{x}_\gamma} = diag(\mathbf{x}_\gamma(1), \mathbf{x}_\gamma(2), \cdots, \mathbf{x}_\gamma(N^t)). \tag{11}$$

Here N^t is the total number of pixels in a 2-D image and *diag*(.) is a diagonal matrix.

Each element, $\mathbf{e}_{ij}(\rho)$ in the error vector represents the cross-relation error between the i-th and j-th channels for a particular pixel position, $\mathbf{r}_\rho$ which is *independent* of the pixels from any other locations as shown below.

$$\mathbf{e}_{ij}(\rho) = \mathbf{x}_o(\rho) \cdot (\hat{\mathbf{s}}_i(\rho) \cdot \hat{\mathbf{s}}_j(\rho) - \hat{\mathbf{s}}_j(\rho) \cdot \hat{\mathbf{s}}_i(\rho)) \tag{12}$$

This makes the error minimization process as well as the solution *pixel position-wise* independent. Therefore, the algorithm is developed to minimize the errors in all the pixel locations simultaneously by excluding the case $\mathbf{e}_{ii} = 0$ and counting the pair, $\mathbf{e}_{ij} = -\mathbf{e}_{ji}$ only once. Thus we have $M(M-1)/2$ distinct error signals [26] and summing up their energies a cost function can be defined as

$$J = \sum_{i=1}^{M-1} \sum_{j=i+1}^{M} \mathbf{e}_{ij}^H \mathbf{e}_{ij} \tag{13}$$

Minimizing the cost function, J in Eq. (13), a unique solution for the γ-th coil map can be obtained for full coil data as

$$\hat{\mathbf{s}}_\gamma = \arg \min_{\mathbf{s}_\gamma} J \tag{14}$$

However, Eq. (14) can be used when fully sampled k-space data are available. For variable density (VD) data, we have to modify Eq. (14) since in VD acquisition [27], the distal high-frequency region of the k-space is under-sampled with larger Δk (spacing between the k-space lines) than that of the fully sampled central lines as shown in Fig. 3 (b). As a result, the image space FOV of the under-sampled high

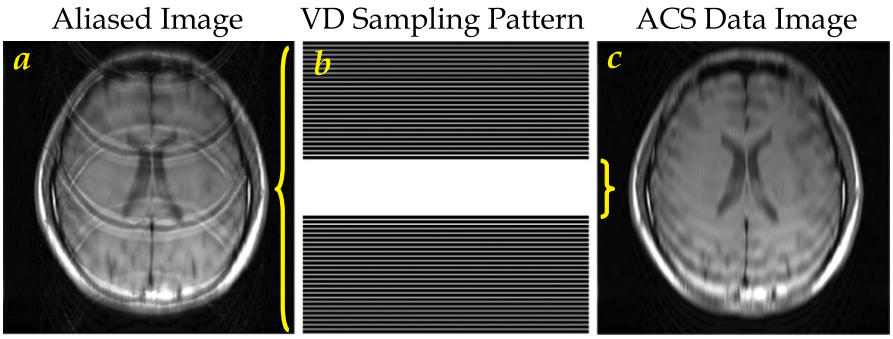

Fig. 3. VD acquisition of MR data: (a) aliased image resulting from VD sampling, (b) VD sampling pattern on the *k*-space and (c) low resolution image with truncation artifact constructed from the fully sampled ACS.

frequency *k*-space region will be smaller than that from the fully sampled auto-calibration-signal (ACS) region producing an aliased image as shown in Fig. 3 (a). Therefore, only the ACS is considered during coil-map estimation by low-pass filtering the *k*-space domain with a filter pass-band equal to the width of the ACS. As a result of this filtering, we obtain a low resolution image, $\widetilde{\mathbf{X}}_\gamma$ with truncation artifact [24] in the image-domain [see Fig. 3 (c)] as

$$\widetilde{\mathbf{X}}_\gamma = (\mathbf{X}_o \cdot \mathbf{S}_\gamma) \otimes \mathbf{W},\ \gamma = 1, 2, \cdots, M. \tag{15}$$

Here, $\otimes$ denotes 2-D circular convolution [28] between the full coil image and the inverse Fourier transform, **W** of the truncation window [29] (Hanning in the proposed method) used to isolate the ACS lines. It is evident from Eqs. (1) and (15) that SOS normalization of $\mathbf{X}_\gamma$ and $\widetilde{\mathbf{X}}_\gamma$ using Eq. (7) will *never* provide the same coil maps thus lose the *consistency*.

As shown in [28], the pixels in the accelerated direction are circularly convoluted with a complex valued window (inverse Fourier transform of the Hanning window in the proposed case) which has the absolute value representation as shown in Fig. 4 by the blue solid line. From the figure we see that around 80 neighborhood pixels (for ACS = 20) are summed up with different weights in the low resolution image constructed from the ACS data. Since the transform matrix associated with the circular convolution is singular, an iterative approach has to be taken to compensate for the circular convolution and to restore closest to the fully sampled coil-data, $\mathbf{X}_\gamma$ from $\widetilde{\mathbf{X}}_\gamma$.

To explain the iterative process, we need to express the low resolution image vector, $\widetilde{\mathbf{x}}_\gamma$ in terms of the weighted sum of the original coil image pixels with the weights, **w** (shown by the blue line in Fig. 4) of the convolution window as

$$\widetilde{\mathbf{x}}_\gamma(\rho) = \mathbf{x}_\gamma(\rho) + \sum_{i=-N/2, i\neq 0}^{N/2-1} \mathbf{w}(i)\mathbf{x}_\gamma(\rho + i) \tag{16}$$

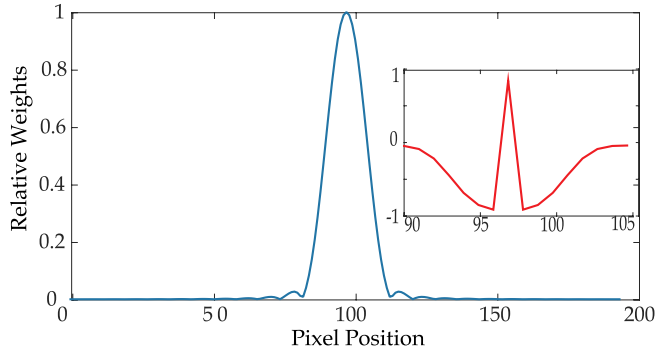

Fig. 4. Convolution window for ACS of 20 (blue-solid line) and the correction filter (Inset) for data sharpening.

where $\mathbf{w}(0) = 1$ is the maximum value of the weights and the number of rows in the image is *N* (which is considered even here without loss of generality). From Eq. (16) we see that the error is actually contributed by the summation term which accounts for the fractions of the neighborhood pixels which are summed with the original pixel at a particular pixel position. Now, re-arranging Eq. (16) we get $\mathbf{x}_\gamma(\rho)$ however it requires $\mathbf{x}_\gamma(\rho + i)$'s.

$$\mathbf{x}_\gamma(\rho) = \widetilde{\mathbf{x}}_\gamma(\rho) - \sum_{i=-N/2, i\neq 0}^{N/2-1} \mathbf{w}(i)\mathbf{x}_\gamma(\rho + i) \tag{17}$$

Therefore, substituting $(\rho + i)$ instead of (ρ) we can approximate the neighborhood pixels $\mathbf{x}_\gamma(\rho + i)$'s recursively as

$$\mathbf{x}_\gamma(\rho + i) = \widetilde{\mathbf{x}}_\gamma(\rho + i) - \sum_{i=-N/2, i\neq 0}^{N/2-1} \mathbf{w}(i)\mathbf{x}_\gamma(\rho + 2i). \tag{18}$$

Thus we can approximate Eq. (16) by substituting $\mathbf{x}_\gamma(\rho + i), i \neq 0$ with the approximated values as

$$\widetilde{\mathbf{x}}_\gamma(\rho) \cong \mathbf{x}_\gamma(\rho) + \sum_{i=-N/2, i\neq 0}^{N/2-1} \widetilde{\mathbf{w}}(i)\widetilde{\mathbf{x}}_\gamma(\rho + i). \tag{19}$$

Here $\widetilde{\mathbf{w}}(i)$ represents the accumulation of the coefficients corresponding to $\widetilde{\mathbf{x}}_\gamma(\rho + i)$ because of the recursive substitution. Values of $\widetilde{\mathbf{w}}(i)$ can be calculated beforehand since those depend only on the $\mathbf{w}(i)$'s with $-N/2 \le i \le N/2$.

Therefore using a filter (inset of Fig. 4) constructed from the negative of $\widetilde{\mathbf{w}}(i)$, $i \neq 0$, on the low resolution data, the summation term (error) in Eq. (16) can be sufficiently eliminated. As a result, effect of convolution is compensated significantly both visually and in NPM scale (a measure of closeness defined in Eq. (41)) from −9 dB for uncorrected image to −13 dB after correction referred to the full-coil image [see Fig. 5]. This improvement eventually increases the consistency of the estimated coil maps without going for coil-map re-estimation as like in [11,28].

Now if the number of ACS lines are sufficient so that the assumption that the bandwidth of the coil sensitivity function is less than that of the low resolution window, the coil-map can be taken out of it [27] as

$$\widetilde{\mathbf{X}}_\gamma \cong (\mathbf{X}_o \otimes \mathbf{W}) \cdot \mathbf{S}_\gamma = \widetilde{\mathbf{X}}_o \cdot \mathbf{S}_\gamma. \tag{20}$$

Here, $\gamma = 1,2,\ldots,M$, and $\widetilde{\mathbf{X}}_o$ is the low resolution object image filtered by **W**. Reproducing all the equations from Eqs. (9) to (13) by substituting $\mathbf{x}_\gamma$ by $\widetilde{\mathbf{x}}_\gamma$ and $\mathbf{x}_o$ by $\widetilde{\mathbf{x}}_o$, the coil maps can be estimated by minimizing $\widetilde{J}$ as

$$\hat{\mathbf{s}}_\gamma \cong \arg\min_{\mathbf{s}_\gamma} \widetilde{J} \tag{21}$$

where $\widetilde{J}$ is the cost function corresponding to the cross-relation error of the truncated data defined by

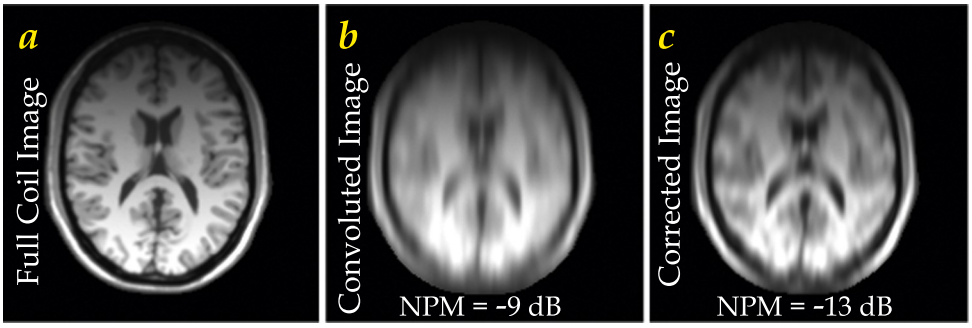

Fig. 5. Effect of re-filtering the low resolution image: a) full coil-data needed for consistent coil-map estimation, b) circularly convoluted low resolution image generated from 20 ACS lines and c) corrected image after re-filtering.

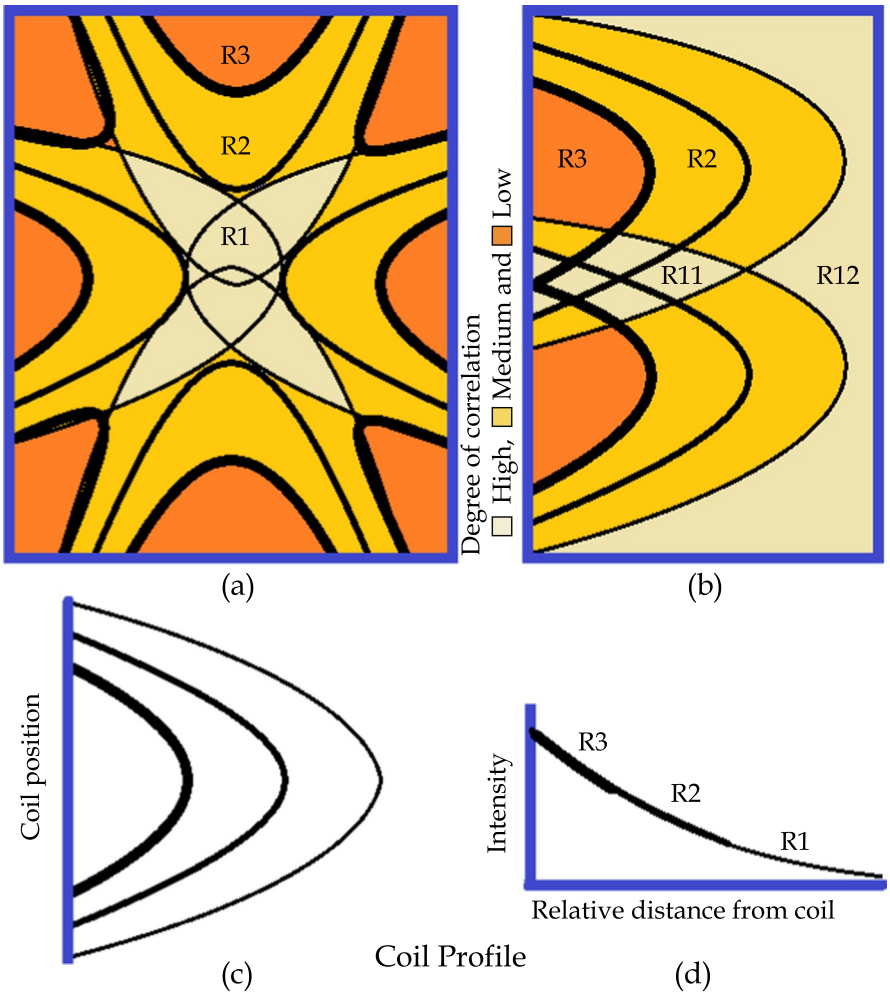

Fig. 6. Spatial correlation among coils: a) bird-cage coil setup, b) surface coil setup, c) spatial signal strength distribution, and d) relative intensity with respect to the distance from the coil.

$$\widetilde{J} = \sum_{i=1}^{M-1} \sum_{j=i+1}^{M} \tilde{\mathbf{e}}_{ij}^{H} \tilde{\mathbf{e}}_{ij} \tag{22}$$

and the cross-relation error for the truncated data is

$$\tilde{\mathbf{e}}_{ij} = \mathbf{D}_{\tilde{\mathbf{x}}_i} \hat{\mathbf{s}}_j - \mathbf{D}_{\tilde{\mathbf{x}}_j} \hat{\mathbf{s}}_i,\ i, j = 1, 2, \cdots, M,\ i \neq j. \tag{23}$$

For cost minimization, an image domain multi-channel LMS (iMCLMS) algorithm [30] with the (n + 1)-th update equation

$$\hat{\mathbf{s}}_\gamma(n+1) = \hat{\mathbf{s}}_\gamma(n) - \mu^{opt}(n) \nabla \widetilde{J}_\gamma(n),\ \gamma = 1, 2, \cdots, M \tag{24}$$

is used with adaptive step-size $\mu^{opt}(n)$ defined by [31]

$$\mu^{opt}(n) = \frac{\hat{\mathbf{s}}^H(n) \nabla \widetilde{J}(n)}{\| \nabla \widetilde{J}(n) \|^2} \tag{25}$$

and the gradient of the cost function, $\nabla \widetilde{J}_\gamma(n)$ as defined by

$$\nabla \widetilde{J}_\gamma(n) = \frac{\partial \widetilde{J}(n)}{\partial \hat{\mathbf{s}}_\gamma^*(n)} = \sum_{i=1}^{M} \mathbf{D}^*_{\mathbf{x}_i^{low}} \tilde{\mathbf{e}}_{i\gamma}(n). \tag{26}$$

Here * denotes the complex conjugate of the pixel elements.

Since minimization of the cross-relation error and hence the update of the coil maps at different pixel-locations are independent, for computational convenience, M coil sensitivity vectors are concatenated into

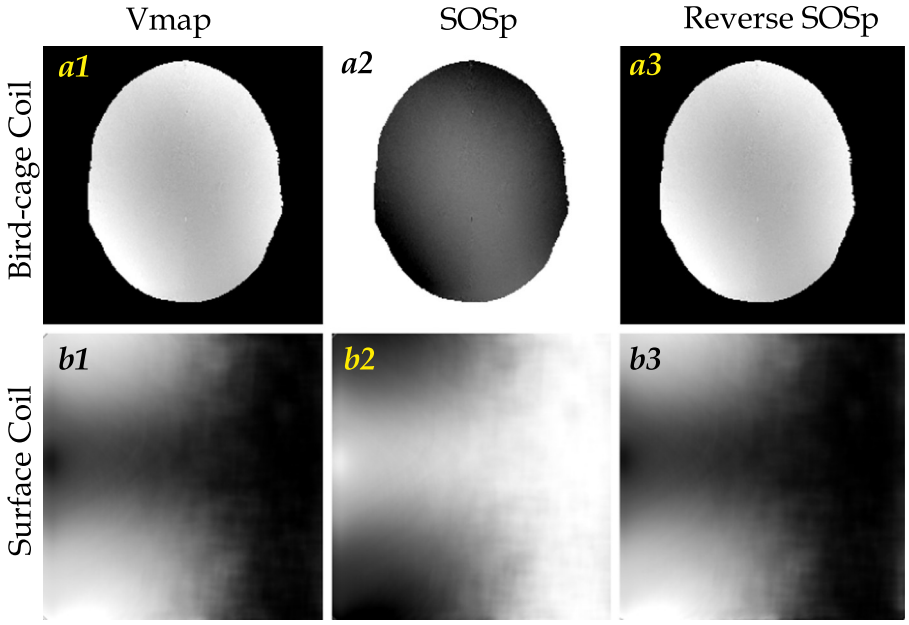

Fig. 7. Relation between **Vmap** and primary coil-SOS: (a1–b1) **Vmap**, (a2–b2) primary coil-SOS and (a3–b3) reverse SOS for bird-cage and surface coil setup.

a larger one, and the update equation for the iMCLMS algorithm thus becomes

$$\hat{\mathbf{s}}(n+1) = \frac{\hat{\mathbf{s}}(n) - \mu^{opt}(n)\nabla\widetilde{J}(n)}{\|\hat{\mathbf{s}}(n) - \mu^{opt}(n)\nabla\widetilde{J}(n)\|} \tag{27}$$

where

$$\hat{\mathbf{s}}(n) = [\hat{\mathbf{s}}_1^T(n) \quad \hat{\mathbf{s}}_2^T(n) \quad \cdots \quad \hat{\mathbf{s}}_M^T(n)]^T$$
$$\nabla\widetilde{J}(n) = [\nabla\widetilde{J}_1^T(n) \quad \nabla\widetilde{J}_2^T(n) \quad \cdots \quad \nabla\widetilde{J}_M^T(n)]^T$$

and $\|\cdot\|$ denotes the l_2-norm used to avoid the trivial solution with all zeros likewise used in [26].

However without any additional constraint, the estimated coil maps using Eq. (27) exhibit *pixel position-wise* scaling ambiguity since cross-relation error minimization based iMCLMS algorithm is pixel position-wise scale blind [32]. Using the fact that the gradient of the cost function, $\nabla\widetilde{J}(n)$ approaches zero when the algorithm converges, it can be shown for $\mathbf{s}(\mathbf{r}_\rho)$ which is the vector that contains the actual ρ-th pixel values from all the coils, that the estimated vector will be a scaled version of the actual one with the pixel position-wise varying scaling factor $\boldsymbol{\alpha}(\mathbf{r}_\rho)$ defined by

$$\alpha(\mathbf{r}_\rho) = \frac{\hat{\mathbf{s}}_\gamma(\mathbf{r}_\rho, \infty)}{\mathbf{s}_\gamma(\mathbf{r}_\rho)}, \gamma = 1, 2, \cdots, M \tag{28}$$

Here $\hat{\mathbf{s}}_\gamma(\mathbf{r}_\rho, \infty)$ is the *primary* (unconstrained) estimate of the ρ-th pixel of the γ-th coil-map and $\boldsymbol{\alpha}(\mathbf{r}_\rho)$ is the scaling factor which is the same for the $\mathbf{r}_\rho$-th pixel locations of *all* the coil maps however varies with pixel location based on the degree of correlation among the true pixel values as shown in Fig. 6 (a) and (b) for bird-cage coil and surface coil, respectively.

Fig. 6 (c) shows the spatial signal strength distribution for a single coil, and Fig. 6 (d) shows the relative intensity as a function of distance from the coil. Therefore, when such coils are arrayed circularly (for bird-cage setup) or linearly (for surface coil setup) we get three broad regions with different levels of correlation, i.e., high, medium and low in the true coil-SOS as shown in Fig. 6 (a) and (b) namely R1, R2 and R3, respectively. Since the correlation as well as the true coil-SOS values gradually change from the peripheral region to the center of the image in bird-cage coil setup, scaling factor has a *one-to-one* correspondence with the true coil-SOS. On the other hand for surface coil, the correlation is high both in the middle region between two coils as well as at the far end since the signal values from the coils are *equal* for both of these regions [see R11 and R12 in Fig. 6 (b)] which makes the scaling factor to be the same. However, the true coil-SOS values are greater in R11 region than that of in R12 region and thus the *one-to-one* relation is affected here in case of the *highly* correlated regions in surface coil setup.

To explain this phenomenon mathematically and without loss of generality, we can use Eq. (28) for two coil map pixels $\mathbf{s}_i(\mathbf{r}_\rho)$ and $\mathbf{s}_j(\mathbf{r}_\rho)$ having positive distance δ, to write

$$\alpha^2(\mathbf{r}_\rho) = \frac{\hat{\mathbf{s}}_i(\mathbf{r}_\rho, \infty)\hat{\mathbf{s}}_j(\mathbf{r}_\rho, \infty)}{\mathbf{s}_i(\mathbf{r}_\rho)\mathbf{s}_j(\mathbf{r}_\rho)} = \frac{\hat{\mathbf{s}}_i(\mathbf{r}_\rho, \infty)\hat{\mathbf{s}}_j(\mathbf{r}_\rho, \infty)}{\mathbf{s}_i(\mathbf{r}_\rho)(\mathbf{s}_i(\mathbf{r}_\rho) + \delta)} \tag{29}$$

Partial derivative of Eq. (29) with respect to δ gives the following sensitivity relation between the variability of $\boldsymbol{\alpha}(\mathbf{r}_\rho)$ with the closeness of the actual coil-map values as

$$\frac{\partial\alpha(\mathbf{r}_\rho)}{\partial\delta} = \frac{-\mathbf{s}_i(\mathbf{r}_\rho)}{2(\mathbf{s}_j(\mathbf{r}_\rho) + \delta)\delta} \tag{30}$$

From Eq. (30) we see that the rate of change in the value of $\boldsymbol{\alpha}(\mathbf{r}_\rho)$ increases with the increase of the closeness (equivalently with the decrease in δ) of the pixel values among the true coil maps.

Fig. 7 illustrates the direct consequence of Eq. (30) for synthetic coil maps in bird-cage (8 coils) and surface coil (2 coils) setup. Here **Vmap** in Fig. 7 (a1–b1) displays the variance map depicting the spatial distribution of the closeness of the true coil maps' pixels defined by

$$\mathbf{Vmap}(\mathbf{r}_\rho) = var([\mathbf{s}_1(\mathbf{r}_\rho), \mathbf{s}_2(\mathbf{r}_\rho), \cdots, \mathbf{s}_M(\mathbf{r}_\rho)]) \tag{31}$$

with *var*(⋯) as the variance function. Since variance is scale dependent, we used SOS normalized coil-maps to calculate the variance map. On the other hand, the primary coil-SOS, $\mathbf{SOS}_p$ generated from the primary coil maps using Eq. (27) is shown in Fig. 7 (a2–b2) as defined by

$$\mathbf{SOS}_p(\mathbf{r}_\rho) = \sqrt{\sum_\gamma |\mathbf{s}_\gamma(\mathbf{r}_\rho, \infty)|^2} \tag{32}$$

From Fig. 7 it is seen that the primary coil-SOS has indeed the reverse contrast of the variance map as a direct consequence of Eq. (30) that is the scaling factor increases with the increase in the closeness of the coil-map pixels. For better understanding of the reverse contrast, we also

show the reverse SOS (difference of $\mathbf{SOS}_p$ from unity) in Fig. 7 (a3–b3).

Now to estimate the true coil-SOS we need to undo the effect of $\boldsymbol{\alpha}(\mathbf{r}_\rho)$ as the true and the primary coil-SOS are related according to Eq. (28) by

$$\mathbf{SOS}_p(\mathbf{r}_\rho) = \boldsymbol{\alpha}(\mathbf{r}_\rho) \times \mathbf{SOS}_t(\mathbf{r}_\rho) \tag{33}$$

Since the rate of increase of the value of $\boldsymbol{\alpha}(\mathbf{r}_\rho)$ is non-linear with the decrease of δ [see Eq. (30)], an empirical relation can be assumed between $\mathbf{SOS}_t$ and $\mathbf{SOS}_p$ by virtue of the **Vmap** and a parameter $\boldsymbol{\beta}(\mathbf{r}_\rho)$ which will take the effect of varying correlation and the scale blindness, respectively to estimate the true coil-SOS, $\hat{\mathbf{SOS}}$ as

$$\hat{\mathbf{SOS}}_t(\mathbf{r}_\rho) = [1^+ - \mathbf{SOS}_p(\mathbf{r}_\rho)]^{\boldsymbol{\beta}(\mathbf{r}_\rho)\mathbf{Vmap}(\mathbf{r}_\rho)} \tag{34}$$

Here 1^+ is slightly higher than unity to avoid zero in the estimate of true coil-SoS. This intuitive relation in Eq. (34) is based on the following facts. Since, the true coil-SOS has low pixel values in the highly correlated regions, i.e., center of the image in case of bird-cage coil setup [33] or at the distant end in case of surface coil setup, $\mathbf{SOS}_t$ and $\mathbf{SOS}_p$ exhibit reverse contrast. Therefore, the reverse SOS is taken as the basis for true coil-SOS estimation. However, if the signal strength is high enough to produce centrally high valued coil-SOS [34], $\mathbf{SOS}_p$ will be used instead of reverse SOS as the basis. Whatever the basis is, scaling factor is non-linearly varying with the closeness of the pixels for which **Vmap** takes care of the varying exponent in Eq. (34). Finally, $\boldsymbol{\beta}(\mathbf{r}_\rho)$ is used to control the values of the exponent since **Vmap** is scale dependent and calculated from SOS normalized coil-data. Besides, $\boldsymbol{\beta}(\mathbf{r}_\rho)$ is used to distinguish between highly correlated regions (R11 and R12) in case of surface coil setup where they have the same **Vmap** but different true coil-SOS values. In case of birdcage coil, single value of $\boldsymbol{\beta}(\mathbf{r}_\rho)$ produces acceptable result, however, for roughly varying intensity, $\boldsymbol{\beta}(\mathbf{r}_\rho)$ can be tuned for specific regions. This tuning can be done based on visual evaluation of an intermediate reconstructed image. An important point to note is that the tuning of $\boldsymbol{\beta}(\mathbf{r}_\rho)$ is much easier than segmentation based post contrast processing yet produces better results than some noted techniques (details in the result section). This is because segmentation of the normalized and smooth **Vmap** based on different ranges of values is very easy. Then $\boldsymbol{\beta}(\mathbf{r}_\rho)$ can be set differently for different regions if necessary [for details see Section 5].

2.3. Estimation of the true coil maps using c-iMCLMS

After estimating the true coil-SOS using Eq. (34), a constrained-iMCLMS (c-iMCLMS) algorithm for built-in removal of the scaling ambiguity is derived as

$$\hat{\mathbf{s}}_\gamma \cong \arg\min_{\mathbf{s}_\gamma} \widetilde{J} \quad \text{subject to} \sqrt{\textstyle\sum_\gamma |\hat{\mathbf{s}}_\gamma(\mathbf{r}_\rho)|^2} = \hat{\mathbf{SOS}}_t(\mathbf{r}_\rho) \tag{35}$$

A single cost function, J_t then can be formulated using the Lagrange multiplier ϵ that determines the coupling between the original cost function and the penalty function as

$$J_t = \widetilde{J} + \epsilon J_p \tag{36}$$

where the penalty function J_p is defined by

$$J_p = \mathbf{e}_{SOS}^H \mathbf{e}_{SOS} \tag{37}$$

with the SOS error vector $\mathbf{e}_{SOS}$ defined by

$$\mathbf{e}_{SOS}(\rho) = \hat{\mathbf{SOS}}_t(\mathbf{r}_\rho) - \sqrt{\sum_\gamma |\hat{\mathbf{s}}_\gamma(\mathbf{r}_\rho)|^2} \tag{38}$$

Taking partial derivative with respect to the coil-map pixels, we find the gradient of the penalty function as

$$\nabla J_p = \frac{\partial J_p}{\partial \hat{\mathbf{s}}_\gamma(\mathbf{r}_\rho)} = \hat{\mathbf{s}}_\gamma^*(\mathbf{r}_\rho)\left(1 - \frac{\hat{\mathbf{SOS}}_t(\mathbf{r}_\rho)}{\sqrt{\sum_\gamma |\hat{\mathbf{s}}_\gamma(\mathbf{r}_\rho)|^2}}\right) \tag{39}$$

Including ∇J_p in Eq. (27), the update equation for the c-iMCLMS algorithm is obtained as

$$\hat{\mathbf{s}}(n+1) = \frac{\hat{\mathbf{s}}(n) - \mu^{opt}(n)(\nabla\widetilde{J}(n) - \epsilon\nabla J_p(n))}{\|\hat{\mathbf{s}}(n) - \mu^{opt}(n)(\nabla\widetilde{J}(n) - \epsilon\nabla J_p(n))\|} \tag{40}$$

Here, $\mu^{opt}(n)$ is still calculated using Eq. (25) since SOS error is independent of the cross-relation error and the value of the coupling factor, ϵ should be around unity otherwise the solution may deviate from the true coil maps (as observed from different sets of data). For very small ϵ, the final estimate remains close to the primary coil maps thus lose *accuracy*. On the other hand, for large ϵ the cross relation error minimization is less favored resulting in less *consistent* coil maps.

However, as $\hat{\mathbf{SOS}}_t(\mathbf{r}_\rho)$ is unavailable at the beginning of coil-map estimation, we need to perform *two* phases of iterations. In the first phase, ϵ is set to zero (to use Eq. (27) in effect) and the *primary* coil maps are estimated. Then using Eq. (34) with $\boldsymbol{\beta}(\mathbf{r}_\rho)$ equals to unity, $\hat{\mathbf{SOS}}_t(\mathbf{r}_\rho)$ is estimated followed by the second phase of 4–5 iterations with ϵ set to near unity to obtain the true coil maps. Finally, the true coil maps are used along with the VD coil data and CG-SENSE algorithm is applied to reconstruct the auto-contrast corrected images that do not require any post contrast correction. In case of any residual contrast ambiguity, values of $\boldsymbol{\beta}(\mathbf{r}_\rho)$ can be set region-wise differently [see Section 5 for suggested values]. The error that may result due to the approximation in Eq. (34) may not affect the estimate of the coil maps much because of using $\hat{\mathbf{SOS}}_t(\mathbf{r}_\rho)$ as a constraint in Eq. (35). This is used to direct the solution from the minimization of $\widetilde{J}$ to the desired point out of infinite *consistent* solutions (with scaling ambiguity). Fig. 8 shows the flow-chart of the proposed technique at a glance.

3. Materials and methods

3.1. Sources of data

8-Channel simulation coil maps [see Fig. 9] were generated using MATLAB codes [35] and were multiplied on a brain image collected from BrainWeb [36] with 0% inhomogeneity. For synthetic *k*-space coil data generation, [see Fig. 11] MRiLab toolbox was used. The true object image for brain was collected from BrainWeb [36] with 0% inhomogeneity and was inserted as the object image in MRiLab toolbox. Data generation environment consisted of 8-coils and 3-D gradient echo sequence with TE = 5 ms, TR = 7 ms, flip angle = 90°, FOV = 16 cm × 16 cm, matrix size = 192 × 192, and slice thickness of 3 mm. Similarly an image of spine [see Fig. 12] collected from [37] was inserted in the MRiLab toolbox with 4-coils and 3-D gradient echo sequence was used to generate the synthetic *k*-space coil data keeping other specifications the same as before. Finally, 8-channel *in-vivo* brain data [9] [see Fig. 15] was acquired on a 3T scanner at GE Healthcare, Waukesha, WI by using a head channel (*in-vivo*, Gainesville, FL) and a 2-D T1-weighted spin echo. As for the other parameters, TE/TR = 11/700 ms, FOV = 22 cm × 22 cm, number of slice = 10 and matrix size = 256 × 256.

3.2. VD-data generation and image reconstruction

The fully sampled synthetic and *in-vivo* *k*-space datasets were manually under-sampled uniformly in the phase encode direction outside of the central ACS lines for generating VD-MR data with ORF 2, 3 and 4. For image reconstruction using GRAPPA and non-linear (NL) GRAPPA, MATLAB code [38] collected from **Parallel MRI Toolbox** was used. For image reconstruction using GSENSE and the proposed method, the same Conjugate Gradient based SENSE (CG-SENSE) routine

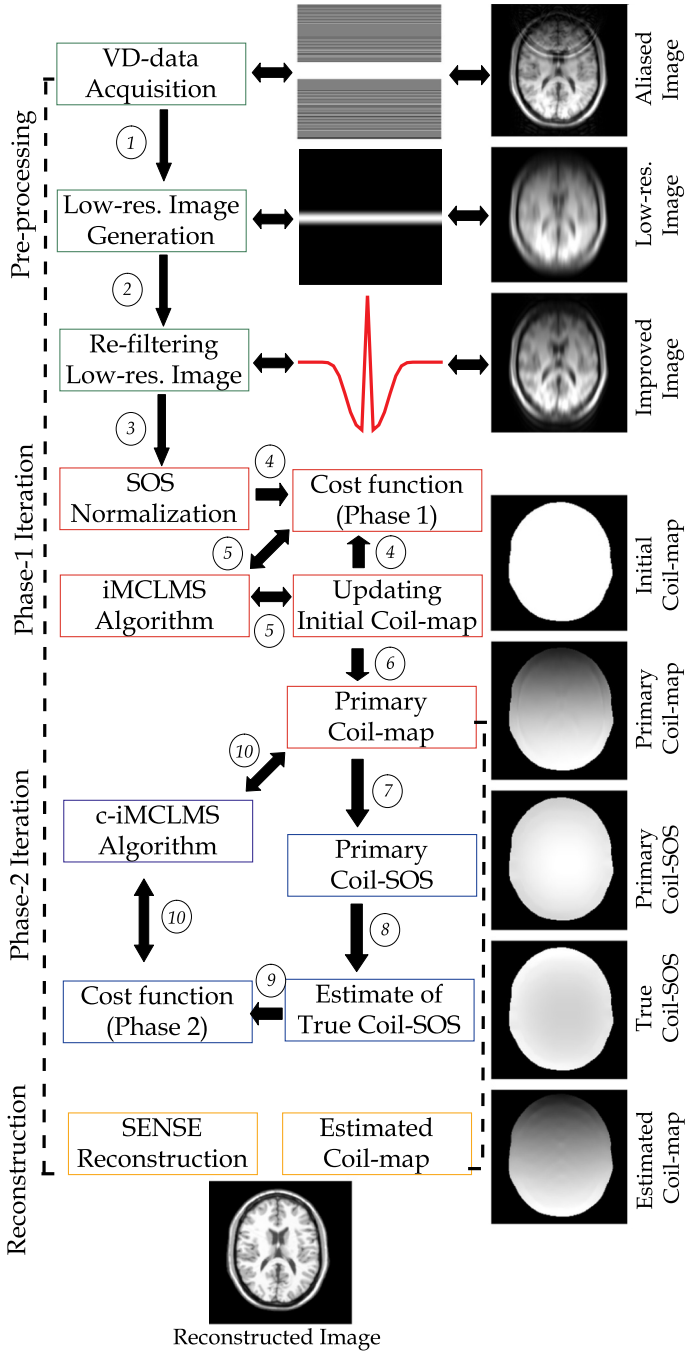

Fig. 8. Block diagram of the proposed method with the sequence shown by the numbers and changes in the image domain alongside the arrows.

was used except that the coil maps were estimated by the SOS method from low resolution data as in [6] for GSENSE, whereas the proposed method used the estimated coil maps generated using Eq. (40) proposed in this paper.

The contrast of the conventional SOS reconstructed images was corrected using the multiplicative approach of MICO toolbox [39] with default number of regions being 2 and fuzzifier parameter set to 3 for 10 number of iterations. However, tuning those parameters in the closest neighborhood did not provide any better reconstruction. For the proposed method, Eq. (34) is used with respective **Vmap** and $\mathbf{SOS}_p$ while the scaling parameter $\boldsymbol{\beta}(\mathbf{r}_\rho)$ was tuned between 0.2 and 1.0 (following the guideline in Section 5) based on visual evaluation of contrast uniformity of the reconstructed images. No additional post-contrast correction was used afterwards.

3.3. Performance evaluation

Since true coil maps, $\mathbf{s}$ were available for the simulation data, to quantify the accuracy of the estimated coil maps, $\hat{\mathbf{s}}$, we used the Normalized Projection Misalignment (NPM) parameter [40] defined as

$$\mathrm{NPM} = 20\log_{10}\left(\frac{\|\zeta\|}{\|\mathbf{s}(\mathbf{r}_\rho)\|}\right) \tag{41}$$

$$\zeta = \mathbf{s} - \frac{\mathbf{s}^T\hat{\mathbf{s}}}{\hat{\mathbf{s}}^T\hat{\mathbf{s}}}\hat{\mathbf{s}} \tag{42}$$

And the *g*-factor map was generated using Eq. (5) as like in [6].

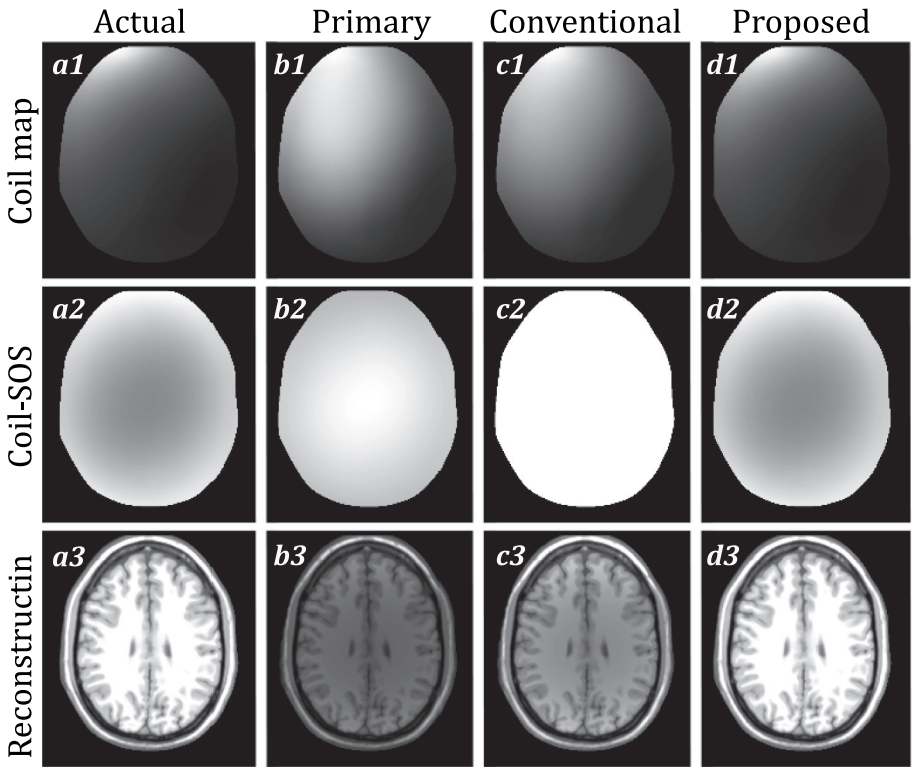

Fig. 9. Results on simulation data: a1–a3) actual, b1–b3) primary, c1–c3) conventional and d1–d3) proposed coil-map, coil-SOS and reconstruction, respectively.

For the synthetic data, the true object image as gold standard was available. Therefore, image artifact was quantified as SANR in dB as defined by

$$\mathrm{SANR} = 10\log_{10}\left(\frac{\sum_{\mathbf{r}_\rho}|\mathbf{x}_0(\mathbf{r}_\rho)|^2}{\sum_{\mathbf{r}_\rho}||\hat{\mathbf{x}}_0(\mathbf{r}_\rho)| - |\mathbf{x}_0(\mathbf{r}_\rho)||^2}\right)\ \mathrm{dB} \tag{43}$$

with $\mathbf{x}_0$ and $\hat{\mathbf{x}}_0$ denoting the true image and the reconstructed image, respectively, both in the same magnitude scale. Maximum achievable SANR at any ORF taking *g*-factor, $\mathbf{g}(\mathbf{r}_\rho)$ in consideration is calculated as

$$\mathbf{SNR}_{PI}(\mathbf{r}_\rho) = \frac{\mathbf{SNR}_{full}(\mathbf{r}_\rho)}{\mathbf{g}(\mathbf{r}_\rho)\sqrt{R_{eff}}} \tag{44}$$

Here $\mathbf{SNR}_{full}$ and $\mathbf{SNR}_{PI}$ are the signal-to-noise ratio for the reconstructed images without and with acceleration, respectively, and the effective reduction factor, R_{eff}, is defined by

$$R_{eff} = \frac{N_{ph}\times R}{N_{ph} + (R-1)\times N_{acs}} \tag{45}$$

where R is the ORF, N_{ph} represents total number of Phase-Encode-Lines and N_{acs} represents the number of ACS lines. We set $\mathbf{g}(\mathbf{r}_\rho)$ to unity in Eq. (44) to calculate the theoretical limit for SANR.

To evaluate the structural similarity of the reconstructed images with the reference for *in-vivo* dataset, Structural SIMilarity (SSIM) index was calculated in addition to SANR. SSIM for two images $\mathbf{x}$ and $\mathbf{y}$ of the same size is defined by

$$\mathrm{SSIM}\left(\mathbf{x},\mathbf{y}\right) = \frac{(2\mu_x\mu_y + c1)(2\sigma_{xy} + c2)}{\left(\mu_x^2 + \mu_y^2 + c1\right)\left(\sigma_x^2 + \sigma_y^2 + c2\right)} \tag{46}$$

where μ and σ^2 are the mean and variance of the respective images and σ_{xy} is the covariance between them with $c1$ and $c2$ being constant parameters.

All the numerical analysis for this research was carried out with MATLAB® (MathWorks, Natick, MA, USA).

4. Results

4.1. Results on simulation data

Fig. 9 (a1–a3) shows one of eight simulation coil maps, their *non-uniform* coil-SOS and the true object image, respectively. Using Eq. (27) on *full* coil-data we obtained the primary coil maps having pixel position-wise scaling ambiguity, their contrast reversed coil-SOS and the corresponding reconstruction as shown by Fig. 9 (b1–b3), respectively. It should be noted that the pixel-variation of the true coil-SOS is reversely *traced* in the primary coil-SOS. However, the conventional coil maps shown in Fig. 9 (c1) estimated by SOS normalization using Eq. (7) have *uniform* coil-SOS [see Fig. 9 (c2)] from which no information about true coil-SOS is *extractable*. As a result, the average NPM between the conventional and true coil maps is below −12 dB and the resulting SOS reconstruction is masked by the true coil-SOS as shown in Fig. 9 (c3) which requires additional post contrast correction. However, using Eq. (34) with $\mathbf{SOS}_p$ and the **Vmap** along with *pixel-wise* varying $\boldsymbol{\beta}(\mathbf{r}_\rho)$ (feasible for simulation data only), we can estimate the true coil-SOS resulting in the proposed coil maps (−40 dB of average NPM with the

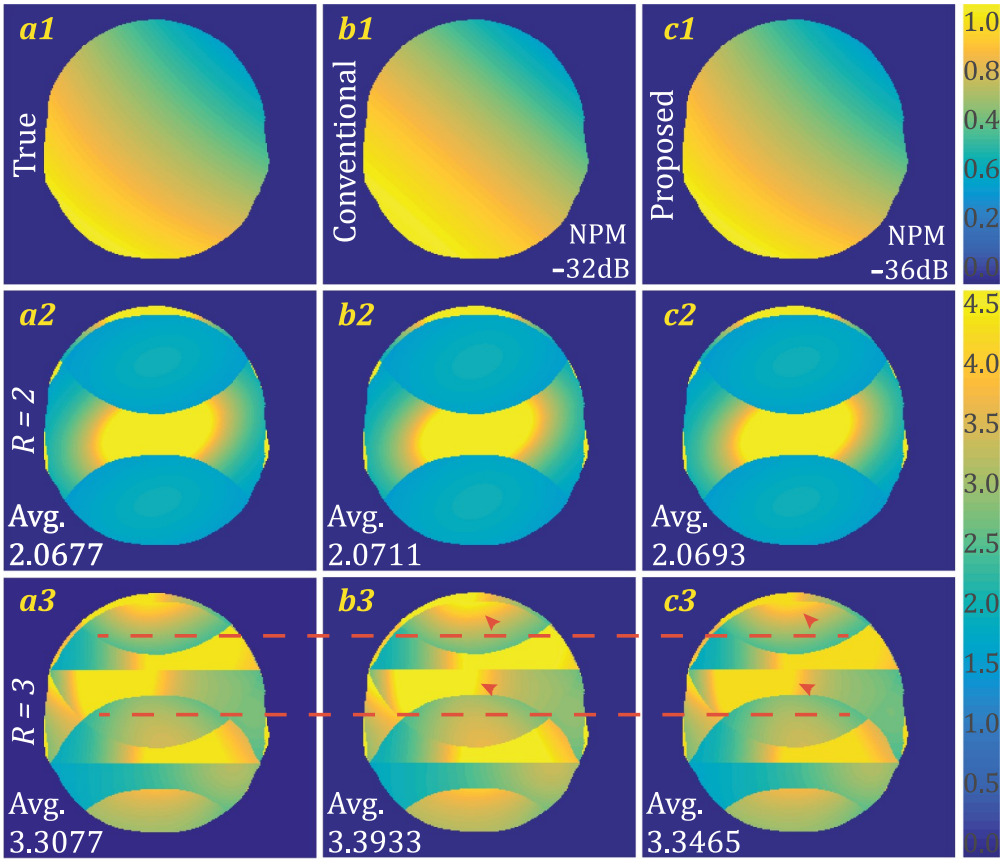

Fig. 10. One of eight coil maps and geometric factor maps at ORF 2 and 3 for (a1–a3) true, (b1–b3) conventional and (c1–c3) proposed coil maps, respectively.

true ones) after second phase of iterations and obtain the true object image without any post-contrast correction [see Fig. 9 (d1–d3)]. However in practice, coil maps have to be estimated from the *low resolution* ACS data with *tuned* values of $\boldsymbol{\beta}(\mathbf{r}_\rho)$ which will degrade the accuracy of the final reconstruction more or less.

Fig. 10 (a1–c1) displays one of eight true coil maps (having uniform coil-SOS), conventional estimate and the proposed estimate, respectively. This time we used coil maps with uniform coil-SOS and the estimation was done from VD data with 20 ACS. The objective of using this data is to demonstrate the novelty of re-filtration by calculating the *g*-maps. Here, *g*-maps for ORF 2 [see Fig. 10 (a2–c2)] and 3 [see Fig. 10 (a3–c3)] are presented for true, conventional and the proposed coil maps, respectively. For ORF 2 we see that the *g*-maps are almost the same with very close average values. However, at ORF of 3, *g*-map for the proposed coil maps is closer to the true *g*-map with less average values than that of the *g*-map for the conventional coil maps. Besides, the variation in the *g*-factor (marked by red arrows) indicates that less noise amplification occurs in case of the proposed coil maps compared to the conventional coil maps. Moreover, the broken lines indicate that the spread of the *g*-factor values for the proposed coil maps is similar to that for the true coil maps. This is because of the re-filtering of the low resolution data for which coil map consistency greatly improves resulting in higher SANR in the reconstructed images.

4.2. Results on synthetic data

Fig. 11 displays the true object image (a) used to produce the synthetic coil data having non-uniform coil-SOS (b) resulting in the SOS image that has severe contrast ambiguity (c). Since the true coil-SOS is centrally high valued, we use $\mathbf{SOS}_p$ directly in Eq. (34) instead of reverse SOS. Besides, this time the estimation of true coil-SOS is done from different ACS data with varying number of segments to demonstrate the effect of choosing regional $\boldsymbol{\beta}(\mathbf{r}_\rho)$ (based on visual evaluation and **Vmap** variation) and the corresponding results are listed in Table 1. From the table we see that the estimation accuracy of the true coil-SOS improves (from -36.8 dB to -39.5 dB) both with the increase of number of segments and ACS lines, however saturates eventually (which is close to the previous result for simulation data). Here the segmentation was done on the normalized **Vmap** and the segments looked like the colored regions in Fig. 11 (b). To obtain the threshold values for the segmentation of **Vmap**, the range of 0 to 1 was uniformly divided by the number of segments and the choice of the values of $\boldsymbol{\beta}(\mathbf{r}_\rho)$ was made based on Section 5.

Both Fig. 13 (a,b) and Table 2 (Brain) show that the SOS reconstructed images by the conventional methods suffer from severe contrast ambiguity resulting in poor SANR referred to the true object image shown in Fig. 11 (a). Image quality is further degraded by the increasing noise at higher ORF from 2 to 4. Note that the SANR values in Table 2 before contrast correction are very poor so as the images in Fig. 13 (a) (a1–a3), (c1–c3) and Fig. 13 (b) (e1–e3) for GSENSE, GRAPPA and NL-GRAPPA, respectively. However, post contrast correction improves the image quality drastically (see the SANR after contrast correction) yet suffer from aliasing (for GSENSE) and distortion (for GRAPPA and NL-GRAPPA) at higher ORF. On the other hand for the proposed auto-contrast-corrected reconstructed images, SANR values are higher than that of the conventional reconstruction (even after post-contrast correction) and closest to the theoretical limit. The theoretical limit is calculated from Eq. (44) with best possible *g*-factor

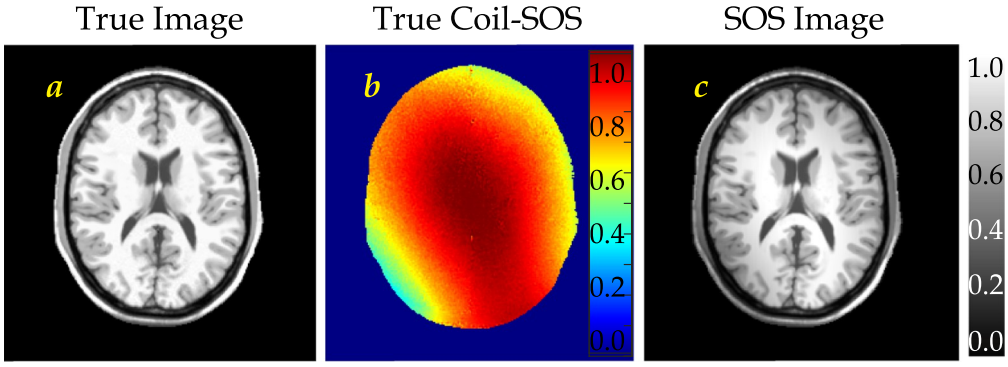

Fig. 11. Synthetic brain: a) true object image with 0% inhomogeneity, b) centrally high valued coil-SOS, and c) resulting SOS image with contrast ambiguity (see that the peripheral region is darker than that of the original).

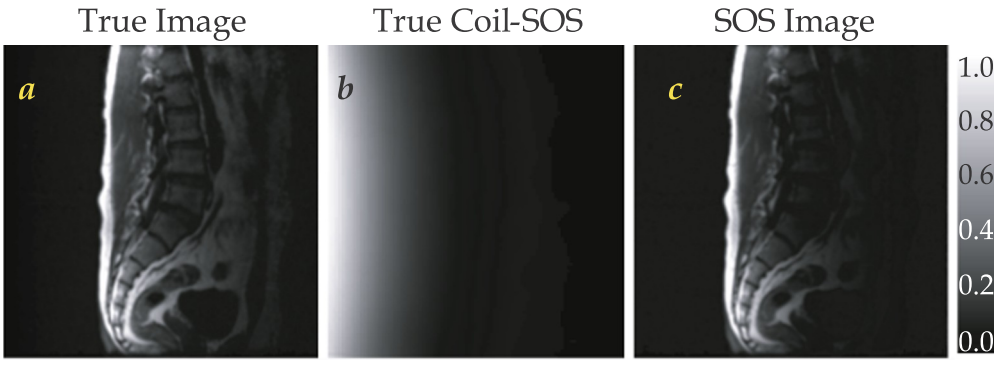

Fig. 12. Synthetic Spine: a) true object image with uniform contrast, b) typical coil-SOS causing surface flare, and c) resulting SOS image with contrast ambiguity (see that the distant region is darker than that of the original).

Table 1
Accuracy in estimation of the true coil-SOS with segmentation and ACS.

Num. of segments	Regional values of $\boldsymbol{\beta}(\mathbf{r}_\rho)$ High < Correlation > Low				NPM (in dB) between $\mathbf{SOS}_t$ and $\hat{\mathbf{SOS}}_t$ for different ACS		
	R1	R2	R3	R4	16	20	32
1	0.24	–	–	–	−36.8	−37.2	−37.7
2	0.25	0.23	–	–	−38.0	−38.3	−38.9
3	0.24	0.23	0.22	–	−38.5	−38.8	−39.3
4	0.25	0.24	0.23	0.22	−38.9	−39.1	−39.5

value, i.e., unity. Thus this result signifies that the proposed method can estimate closest to the true coil maps which in turn produce better reconstructed images closest to the theoretical limit.

Similarly for the spine synthetic data [see Fig. 12 (a)] with non-uniform coil-SOS (b) resulting in a contrast ambiguous SOS image (c), the proposed method also performs better than the conventional methods. Fig. 14 (a,b) and Table 2 (Spine) display the reconstructed images and list the SANR values, respectively. Unlike the brain images, the spine images needed 4 group of segments as shown in Fig. 6 (b) to distinguish between the highly correlated regions with the same scaling factor. Values of $\boldsymbol{\beta}(\mathbf{r}_\rho)$ were chosen as 0.15, 0.5, 0.4, and 0.25 for R11, R12, R2 and R3 regions, respectively, while estimating the true coil-SOS based on **Vmap** and visual comparison. Comparison [see Fig. 14 (a,b) and Table 2] with the other reconstructed images (before/after correction), the proposed reconstruction shows better quality both visually and numerically likewise for the brain images. However, the accuracy level degraded a little compared to that for the brain images because of two reasons. First, the number of coils (4 coils) in the spine data was less than that of the brain data (8 coils) which affects over all SANR of the reconstructed images. Therefore, ORF of 4 is the theoretically highest reduction factor. Second, correlation pattern in spine coils consists of tied regions with different true coil-SOS values. Therefore, accuracy largely depends on the proper choice of scaling/tuning factor $\boldsymbol{\beta}(\mathbf{r}_\rho)$ to distinguish those regions. However, the SANR values are still over the threshold of 'acceptance' (−20 dB) at ORF of 4 and touches to the threshold of 'excellent' (−32 dB) at ORF of 3 [41]. As for the other conventional methods, SANR after ORF of 2 is comparatively poor as seen from Table 2.

4.3. Results on in-vivo data

Fig. 15 (a) displays the SOS image of the *in-vivo* data with contrast inhomogeneity. The associated bias field [see Fig. 15 (b)] measurement and the post-contrast correction were done using MICO toolbox. On the other hand, the proposed technique was applied on the *full* dataset to generate an auto-contrast corrected reconstructed image. Since the true image for visual and numeric evaluation is unavailable, reference image [see Fig. 15 (c)] has been produced by taking the root-mean-square (r.m.s.) sum of both of the contrast corrected images produced by the conventional and the proposed method. Fig. 16 displays the post contrast corrected reconstructed images from *in-vivo* data using GSENSE (a1–a3), GRAPPA (b1–b3), NL-GRAPPA (c1–c3) and the auto contrast corrected proposed reconstruction (d1–d3) at $R = 2$, 3 and 4 for 20 ACS lines. We used 4 segments for coil-SOS estimation in the proposed reconstruction. Table 3 shows the SANR (in dB) and SSIM values of the reconstructed images referred to in Fig. 15 (c) for numeric evaluation. To aid visual evaluation, log-difference images are displayed in Fig. 17

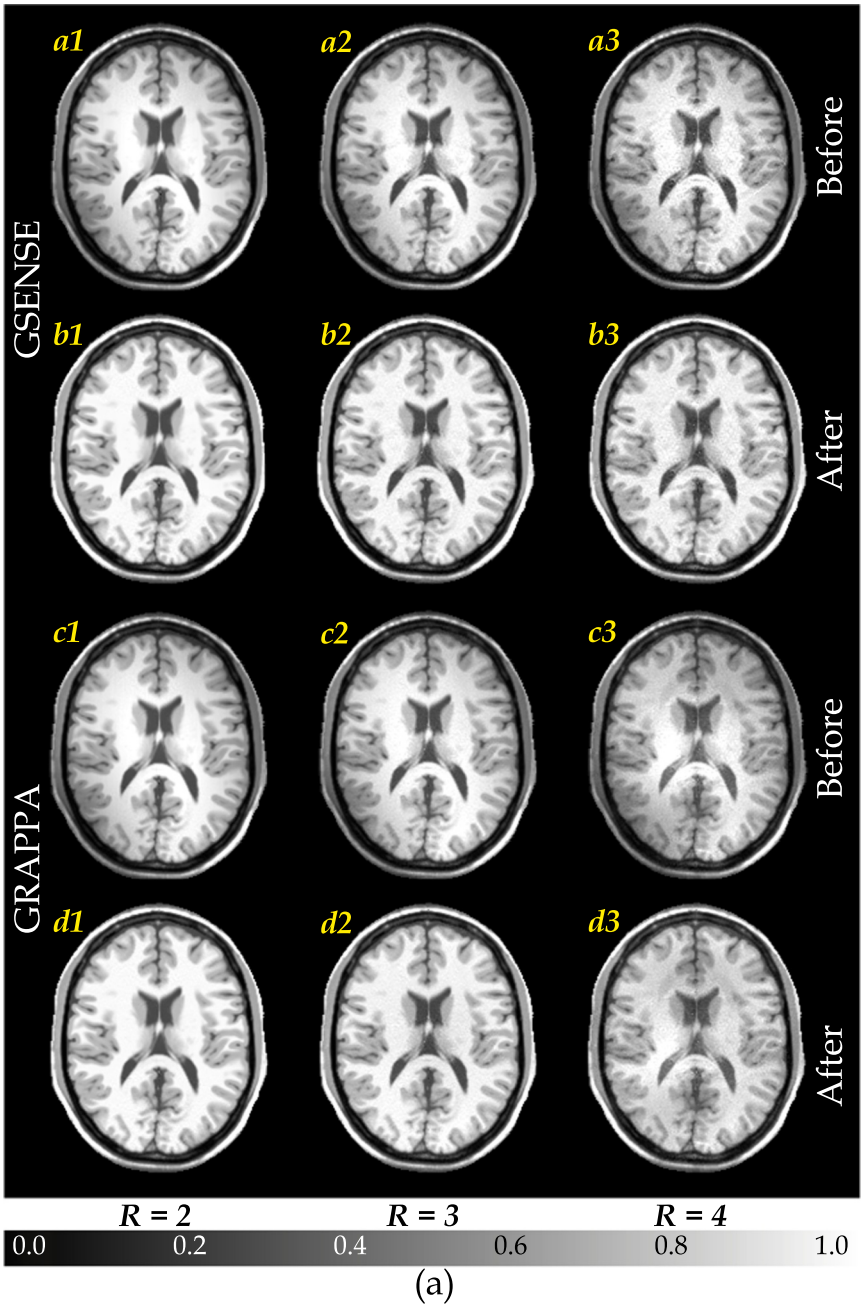

Fig. 13. (a) Brain images (non-uniform coil-SOS of synthetic data) reconstructed by GSENSE (a1–a3/b1–b3), GRAPPA (c1–c3/d1–d3) and (b) NL-GRAPPA (e1–e3/f1–f3) are shown before/after post-contrast correction using [44] along with the proposed auto-contrast corrected reconstruction (g1–g3) from ACS = 20 at R = 2, 3 and 4 for reference image shown in Fig. 11 (a).

accordingly to show the spatially varying noise with respect to ORF.

From Table 3 we see that the SANR values (and the SSIM index) decreases with the increase of R. All the conventional methods have less SANR (and less or equal SSIM) than that of the proposed reconstruction except for GRAPPA at R = 2 (with 1 dB higher SANR) which is not significant since SANR over 32 dB is considered 'excellent' [41] and all the conventional methods are known to produce the same quality images (from visual perception) at R = 2 [3]. Interestingly, only the proposed method exceeds the threshold of 'excellent' (32 dB) at R = 3. Though the SANR is below this threshold at R = 4 for all the methods, yet the proposed reconstruction quality is 9 dB higher than the 'acceptable' limit of 20 dB [41].

Fig. 17 supports the results in Table 3 from noise point of view. As we see that noise pattern is almost the same at R = 2 except for the GSENSE. Fragments of residual aliasing is visible here which is completely absent in case of the proposed method. This improvement is due to the fact that the proposed coil maps are more consistent by virtue of the compensation of the convoluted low resolution images. On the other hand, GRAPPA has less noise than NL-GRAPPA at ORF of 2. However, with the increase of R, only the proposed method maintains

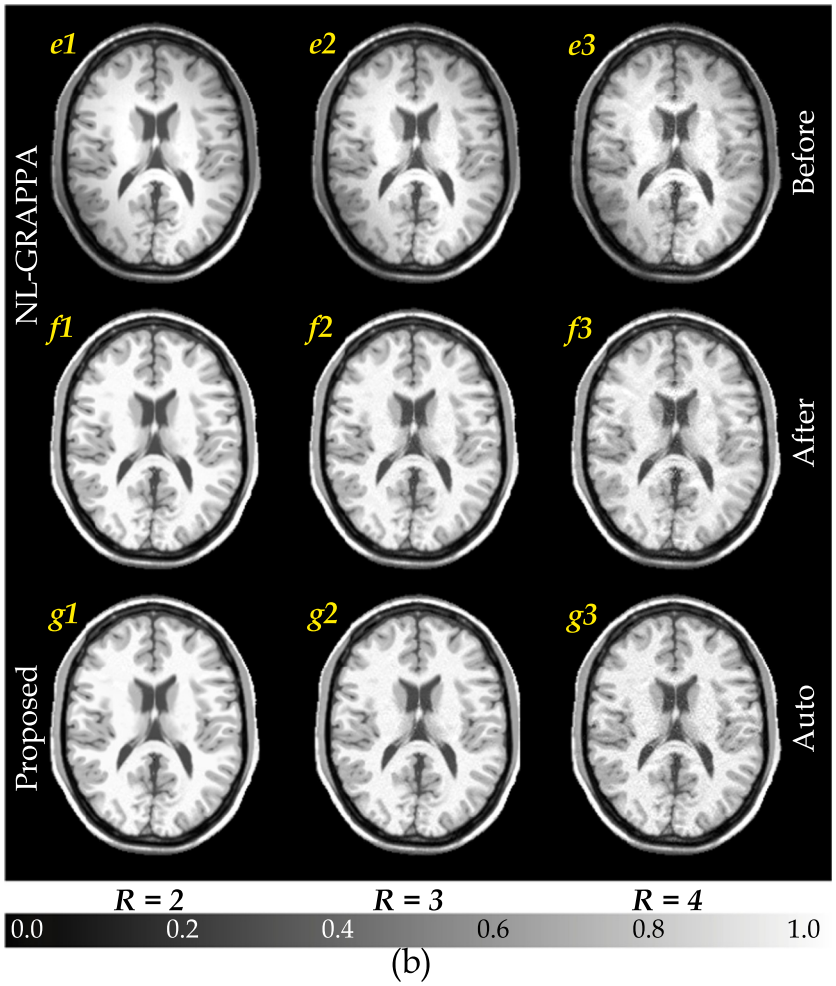

Fig. 13. (*continued*)

Table 2
SANR (in dB) for synthetic brain and spine images with theoretical limits.

Object image	ORF R	Conventional reconstruction						Proposed auto correction	Theoretical limit
		Before correction			After correction				
		GS	GP	NL	GS	GP	NL		
Brain	2	17	20	18	39	39	38	40	41
	3	16	14	16	31	28	30	34	35
	4	14	8	15	26	21	29	30	32
Spine	2	10	11	12	35	36	37	38	39
	3	10	10	10	26	16	27	32	33
	4	9	8	10	22	10	25	26	30

its consistency while GRAPPA and GSENSE suffer the most. At ORF of 4, the recently reported NL-GRAPPA comes closer to the proposed reconstruction however falls short by 1 dB.

Since the reconstructed images at $R = 4$ from 20 ACS lines cannot maintain clinical quality, we increased the ACS to see the improvement. However to maintain R_{eff} equal to that at ORF 3 for 20 ACS lines, maximum ACS was limited to 48. The results are listed in Table 4 and the reconstructed images for 32 ACS (since the SANR crossed 30 dB for ACS = 32) is shown in Fig. 18. From the performance indices, we can say that except for GRAPPA, other three methods including the proposed method equally ripped the benefit from additional ACS lines. However for clinical applications, ACS-ORF combination has to be chosen based on the required quality along with data acquisition speed.

5. Discussions

The proposed technique of coil-map estimation has given excellent results in different simulation, synthetic and *in-vivo* data, however, self-comparison reveals that the reconstructed image quality varies with the imaging object compared to one another. For example, in case of using bird-cage coil for imaging brain, the proposed technique successfully estimated closest to the true coil-maps in all types of datasets. However, low SNR regions in the surface coil setup for imaging object like spine, affect the coil-map values since cross relation error minimization based

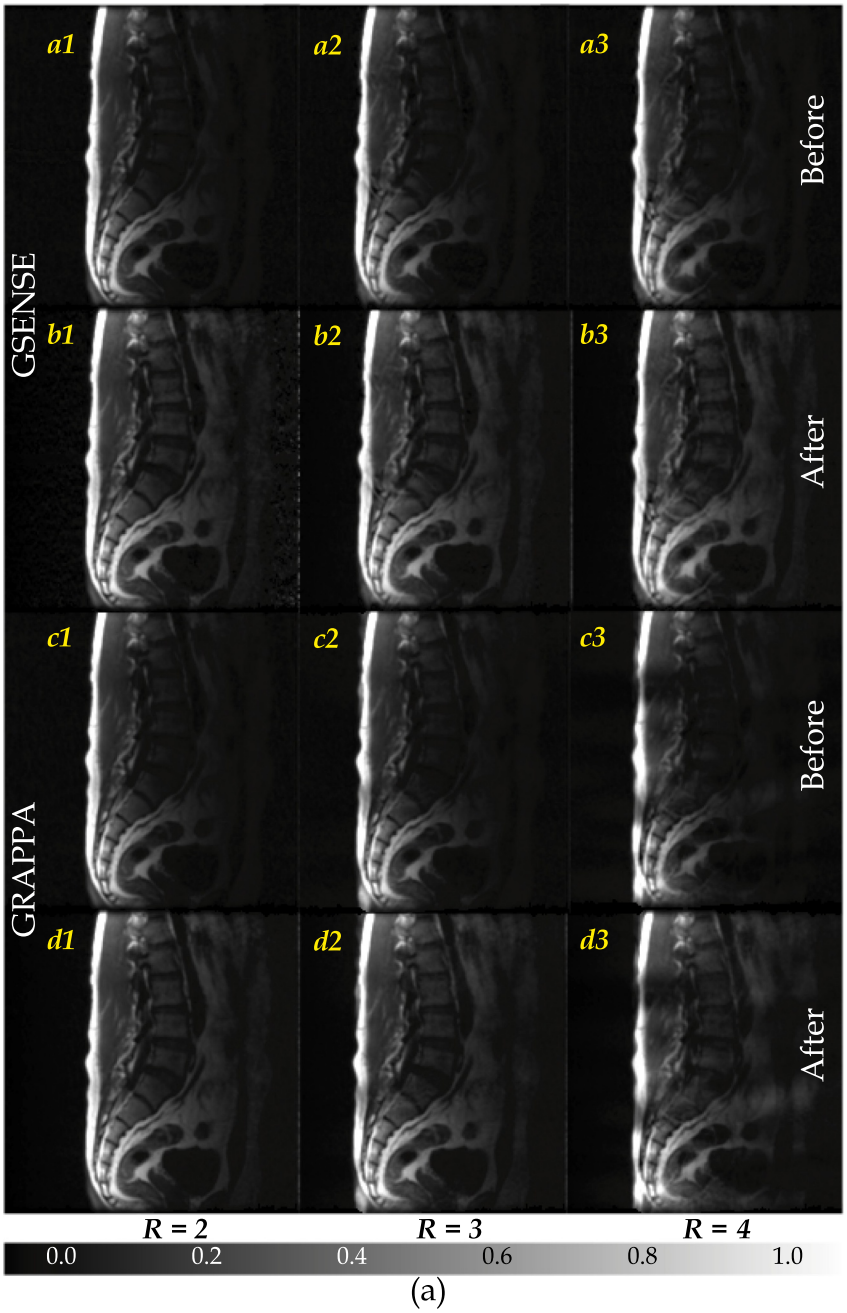

Fig. 14. (a) Spine images (non-uniform coil-SOS of synthetic data) reconstructed by GSENSE (a1–a3/b1–b3), GRAPPA (c1–c3/d1–d3), and (b) NL-GRAPPA (e1–e3/f1–f3) are shown before/after post-contrast correction using [44] along with the proposed auto-contrast corrected reconstruction (g1–g3) from ACS = 20 at R = 2, 3 and 4 for reference image shown in Fig. 12 (a).

iterative method struggles at low valued pixel regions. Yet, the proposed method produces better results even in this case with very low SNR where usually GRAPPA is preferred over SENSE in practice [3] which is actually an inherent drawback of SENSE based reconstruction [2]. Comparison among the conventional methods shows that GRAPPA is found to give better result than NL-GRAPPA at low ORF, however, with the increase of acceleration factor, NL-GRAPPA exhibits better noise immunity than GRAPPA. On the other hand, quality for GSENSE drops pretty fast with the increase of ORF. Only the proposed method showed consistent performance closest to the theoretical limit at every ORF.

However, the performance of the proposed method greatly depends on the coil-map accuracy given that the low resolution coil data are consistent. Therefore, estimation of the true coil-SOS to use it as the SOS constraint plays a vital role in the proposed method. To estimate the true coil-SOS from the primary coil-SOS and the **Vmap**, the following guidelines should be followed. If the variation of the true coil-SOS pixels is *low*, it is found that reverse of $\mathbf{SOS}_p$ is pretty close to the true coil-SOS. Therefore $\boldsymbol{\beta}(\mathbf{r}_\rho)$ should be set element-wise inverse of **Vmap**. In case of *highly* varying contrast as for the images shown in Figs. 13 and 15, values of **Vmap** as the exponent takes care of the non-linear relation between the scaling factor and the true coil-SOS. In this case, one can set $\boldsymbol{\beta}(\mathbf{r}_\rho)$ to be unity in Eq. (34) for all the pixel locations and then visually evaluate the contrast variation across the full image. If the contrast is not corrected with the help of **Vmap**, regional $\boldsymbol{\beta}(\mathbf{r}_\rho)$ can be employed by segmentation of **Vmap** based on the degree of

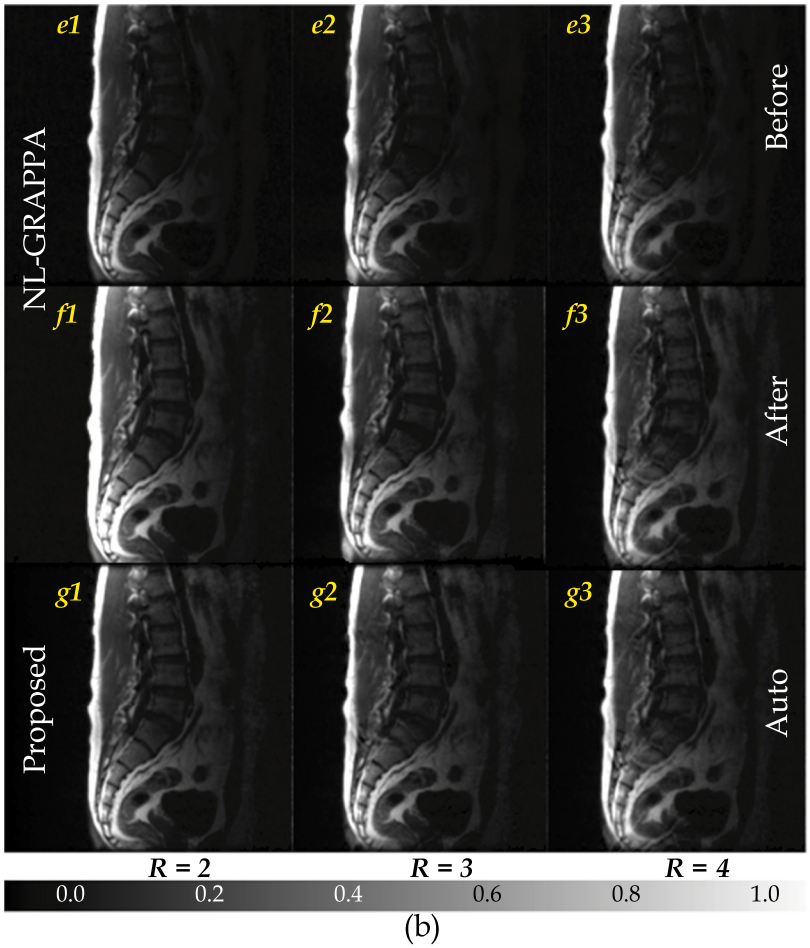

Fig. 14. (*continued*)

correlation (which is a lot easier than segmentation and surface fitting [42] of a fine-detailed SOS reconstructed image). After segmentation, $\boldsymbol{\beta}(\mathbf{r}_\rho)$ is chosen based on the desired change in the estimate of the true coil-SOS. To increase the pixel values for a particular region, $\boldsymbol{\beta}(\mathbf{r}_\rho)$ is to be less than unity and to decrease the pixel values, $\boldsymbol{\beta}(\mathbf{r}_\rho)$ is to be greater than unity since the normalized **Vmap** (value ranging from 0 to 1) is used in association with $\boldsymbol{\beta}(\mathbf{r}_\rho)$. To take the decision on $\boldsymbol{\beta}(\mathbf{r}_\rho)$, an intermediate image can be reconstructed using **Cmap** and visually evaluate the contrast variation. Then the proposed algorithm can be employed to estimate the true coil maps.

Second, the effect of coil-data noise can degrade the final image quality however does not affect the accuracy of the estimated coil-maps. This is due to the fact that the coil maps are estimated using the low resolution coil-data constructed from the ACS where the SNR is pretty high and the high frequency component of the noise is filtered out by the ACS window. Only during the reconstruction, this random noise can affect since random acquisition noise in *k*-space produces random noise in the image space [43]. In the proposed method, random noise is handled in two ways. As the estimation process is pixel position-wise independent, noise outside the object boundary is eliminated by using masks making the pixel values null outside the image boundary. On the other hand, regularization [9] limits the noise propagation within the object while the signal-to-noise-ratio in the center of *k*-space sufficiently suppresses the *k*-space noise [43].

Finally, if the object contains too much void as like in cardiac or abdomen images, estimation accuracy degrades for low SNR in those pixel locations [3]. In this case, GRAPPA guided SENSE could be employed [2]. Besides, improvement in ACS isolating window could further improve the consistency of the estimated coils. It is seen that increase of ACS improves the coil accuracy in expense of reducing the effective ORF. Therefore, research is going on to improve the low resolution data without increasing the ACS for achieving higher SANR without lowering R_{eff}. Besides, low SNR at the distant end from the coil in surface coil setup degrades the SANR of the overall image compared to the bird-cage coil setup which can be improved by further research.

As for the time-cost measurement, we used a computer with CPU: Intel® Core™ i7-8700 K @ 3.70 GHz, RAM: 32 GB on 256 × 256 × 8 size *in-vivo* brain image from 32 ACS lines at ORF = 4. Time requirements for full image reconstruction by GSENSE, GRAPPA, NL-GRAPPA and the proposed method were 0.14 s, 6.41 s, 27.12 s and 0.52 s, respectively.

6. Conclusions

This paper has presented a new blind technique for obtaining Highly Accurate Sensitivity for Auto-contrast-corrected reconstructioN (HASAN) as an improvement of the SENSE based pMRI reconstruction methods. The proposed method has introduced a novel SOS-constraint

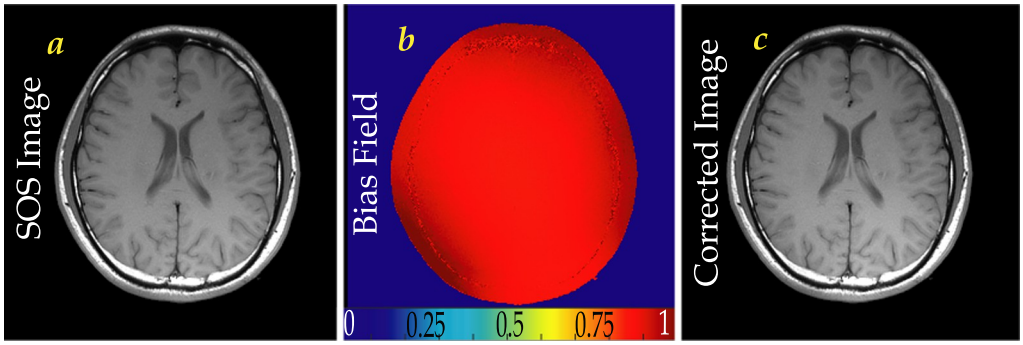

Fig. 15. *In-vivo* brain data: a) SOS image, b) estimated true coil-SOS (bias field), and c) contrast corrected image (reference).

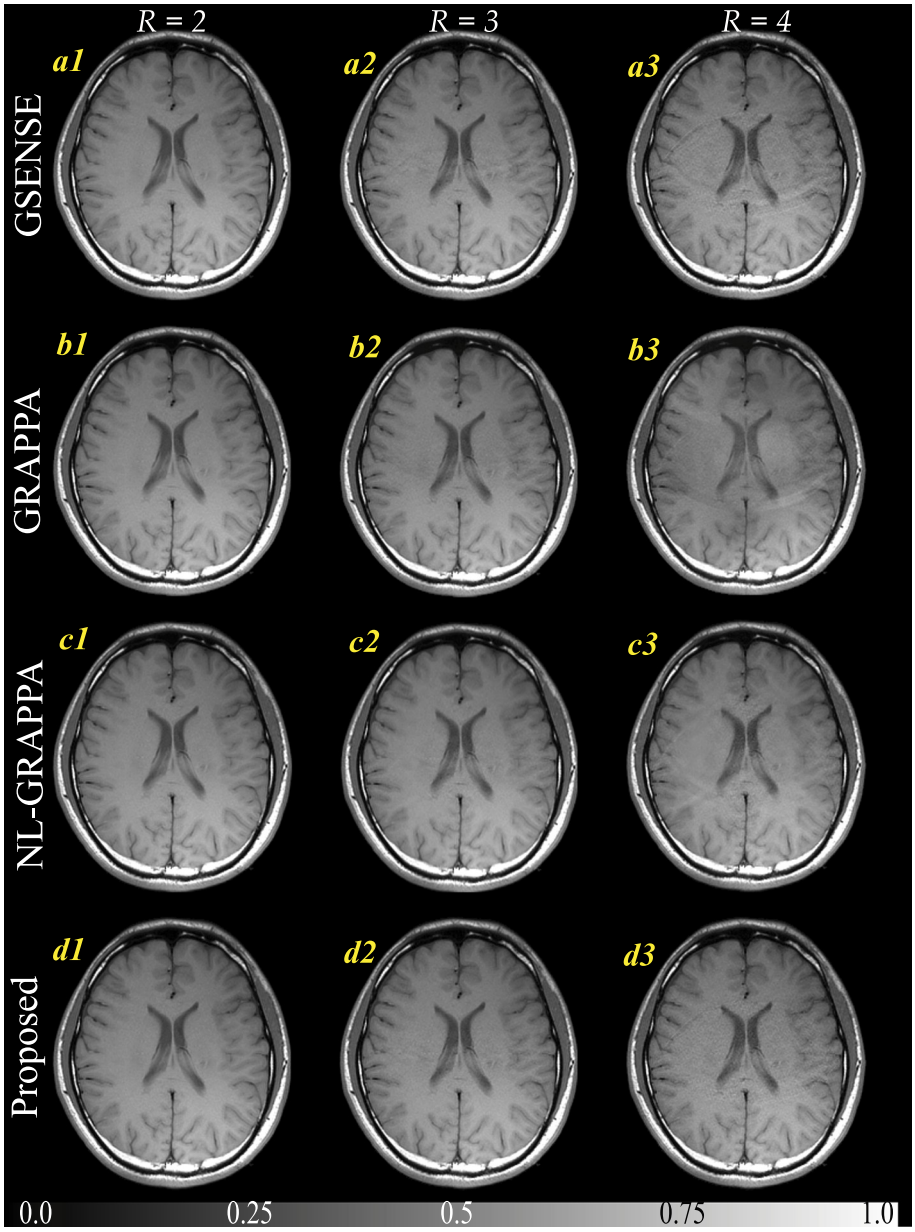

Fig. 16. Brain images reconstructed from *in-vivo* data with GSENSE (a1–a3), GRAPPA (b1–b3), NL-GRAPPA (c1–c3) and the proposed (d1–d3) method. Images are displayed in the same normalized scale.

Table 3
SANR and SSIM for the *in-vivo* brain data with ACS = 20.

	SANR (dB)				SSIM			
R	GS	GP	NL	Prop.	GS	GP	NL	Prop.
2	37	40	36	39	1.000	1.000	1.000	1.000
3	30	29	31	34	0.999	0.998	0.999	1.000
4	25	21	28	29	0.997	0.891	0.998	0.999

to ensure the coil-map accuracy which is absent in the conventional estimation process. As a result, the conventional SOS reconstructed images suffer from severe contrast variation which is usually addressed by adopting additional post-contrast correction schemes in the literature. However, the elegance of the proposed method is that it does not require any such post-contrast correction because of using accurate coil maps which possess the true coil-SOS. The estimation of the true coil-SOS is a built-in process guided by the coil-map correlation and offers a very easy way to accurately determine the contrast variation due to magnetic field inhomogeneity. Then the use of this accurate coil-map directly reconstruct closest to the true object image with true contrast variation. Besides, compensation for the circular convolution to increase data consistency increases the coil-map accuracy resulting in reduced noise amplification at higher reduction factor. As a result, the proposed novel technique gives better reconstructed images compared to the widely used techniques in the literature.

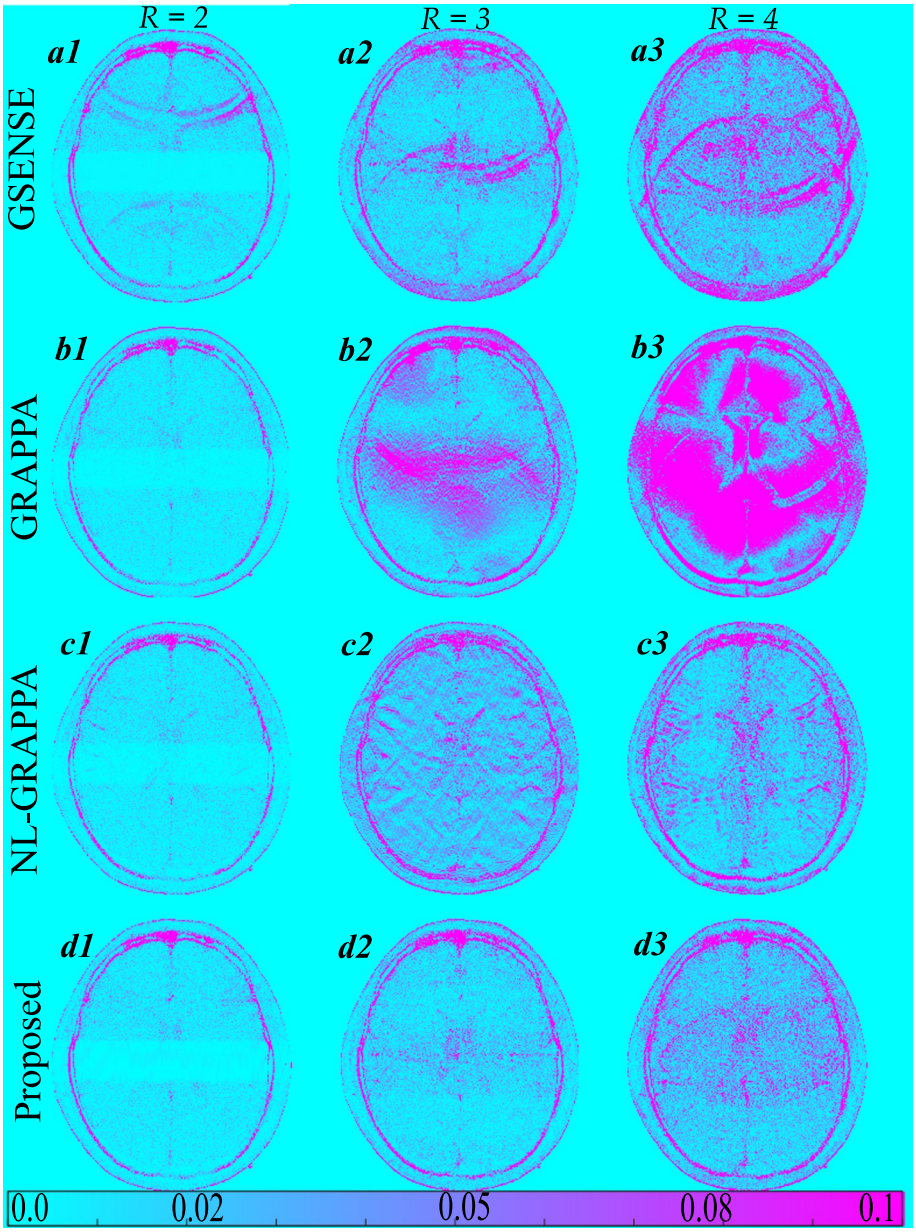

Fig. 17. Log-difference images of the *in-vivo* reconstructed images refereed to the contrast corrected reference image for GSENSE (a1–a3), GRAPPA (b1–b3), NL-GRAPPA (c1–c3) and the proposed (d1–d3) method.

Table 4
SANR and SSIM for the *in-vivo* brain data at ORF = 4.

	SANR (dB)				SSIM			
ACS	GS	GP	NL	Prop.	GS	GP	NL	Prop.
24	27	20	29	29	0.997	0.882	0.998	0.999
32	30	18	30	31	0.997	0.851	0.999	0.999
48	31	16	31	31	0.998	0.825	0.999	0.999

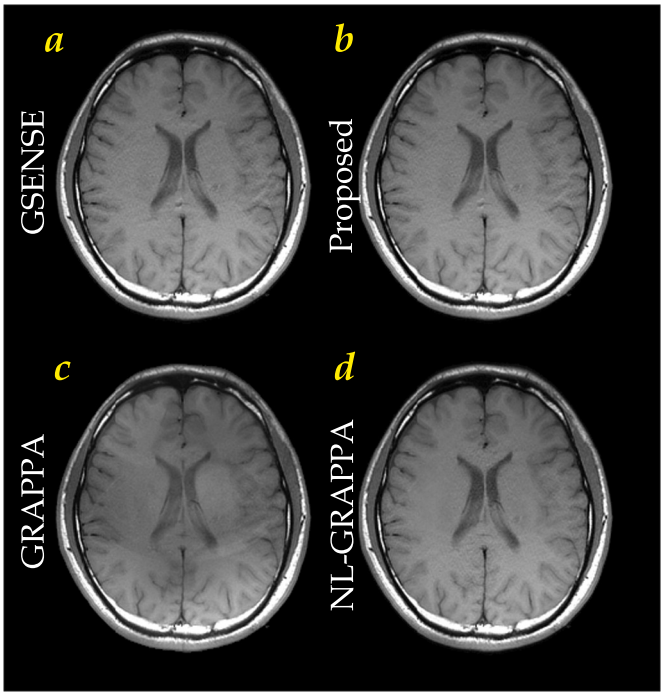

Fig. 18. *In-vivo* brain images from ACS = 32 at ORF = 4. GSENSE (a), proposed (b), GRAPPA (c) and NL-GRAPPA (d) shows improved quality because of the increase of ACS.

References

[1] MRI Physics: Parallel Imaging in MRI, http://xrayphysics.com/parallel.html.
[2] Deshmane A, Gulani V, Griswold MA, Seiberlich N. Parallel MR Imaging. J Magn Reson Imaging 2012;36:55–72. https://doi.org/10.1002/jmri.23639.
[3] Blaimer M, Breuer F, Mueller M, Heidemann RM, Griswold MA, Jakob PM. SMASH, SENSE, PILS, GRAPPA How to choose the optimal method. Top Magn Reson Imaging 2004;15(4):223–36. https://doi.org/10.1097/01.rmr.0000136558.09801.dd.
[4] Aja-Fernández S, Vegas-Sánchez-Ferrero G. Parametric Noise Analysis in Parallel MRI. Statistical analysis of noise in MRI 2016:211–23. https://doi.org/10.1007/978-3-319-39934-8_10.
[5] Griswold MA, Jakob PM, Heidemann RM, Nittka M, Jellus V, Wang J, Kiefer B, Haase A. Generalized autocalibrating partially parallel acquisitions (GRAPPA). Magn Reson Med 2002;47(6):1202–10. https://doi.org/10.1002/mrm.10171.
[6] Pruessmann KP, Weiger M, Scheidegger MB, Boesiger P. SENSE: sensitivity encoding for fast MRI. Magn Reson Med 1999;42(5):952–62. https://doi.org/10.1002/(SICI)1522-2594(199911)42:5<952::AID-MRM16>3.0.CO;2-S.
[7] Pruessmann KP, Weiger M, Börnert P, Boesiger P. Advances in sensitivity encoding with arbitrary k-space trajectories. Magn Reson Med 2001;46(4):638–51. https://doi.org/10.1002/mrm.1241.
[8] Hestenes MR, Stiefel E. Methods of conjugate gradients for solving linear systems. 1952;49(6).
[9] Liu B, King K, Steckner M, Xie J, Sheng J, Ying L. Regularized sensitivity encoding SENSE reconstruction using Bregman iterations. Magn Reson Med 2009;61(1):145–52. https://doi.org/10.1002/mrm.21799.
[10] Griswold MA, Breuer F, Blaimer M, Kannengiesser S, Heidemann R, Mueller M, et al. Auto-calibrated coil sensitivity estimation for parallel imaging. NMR Biomed 2006;19:316–24. https://doi.org/10.1002/nbm.1048.
[11] Huang F, Chen Y, Yin W, Lin W, Ye X, Guo W, et al. A rapid and robust numerical algorithm for sensitivity encoding with sparsity constraints: self-feeding sparse SENSE. Megn Reson Med 2010;64:1078–88. https://doi.org/10.1002/mrm.22504.
[12] Walsh DO, Gmitro AF, Marcellin MW. Adaptive reconstruction of phased array MR imagery. Magn Reson Med 2000;43(5):682–90. https://doi.org/10.1002/(SICI)1522-2594(200005)43:5<682::AID-MRM10>3.0.CO;2-G.
[13] Altair H, MRI Birdcage Coil Design https://www.feko.info/applications/white-papers/mri-birdcage-coil-design/MRI-birdcage-coil-design.
[14] MR-Technology, Birdcage http://www.mr-tip.com/serv1.php?type=db1&dbs=Bird.
[15] Morrison RL, Jacob M, Do MN. Multichannel estimation of coil sensitivities in parallel MRI. Proc. 4th ISBI. IEEE. 2007. p. 117–20.
[16] Banu R, Ram DAR. Contrast enhancement of MRI images: a review. Int J Emerging Technol Adv Eng 2015;5.
[17] Surface coil flare, http://mriquestions.com/surface-coil-flare.html.
[18] Moyher SE, Vigneron DB, Nelson SJ. Surface coil MR imaging of the human brain with an analytic reception profile correction. J Magn Reson Imaging 1995;5(2):139–44. https://doi.org/10.1002/jmri.1880050204.
[19] Roemer PB, Edelstein WA, Hayes CE, Souza SP, Mueller OM. The NMR phased array. Magn Reson Med 1990;16(2):192–225. doi:The NMR phased array.
[20] Axel L, Costantini J, Listerud J. Intensity correction in surface-coil MR imaging. AJR 1987;148(2):418–20. https://doi.org/10.2214/ajr.148.2.418.
[21] Narayana P, Brey W, Kulkarni M, Sievenpiper C. Compensation for surface coil sensitivity variation in magnetic resonance imaging. Magn Reson Imag 1988;6(3):271–4. https://doi.org/10.1016/0730-725X(88)90401-8.
[22] Gabarda S, Cristóbal G. Blind image quality assessment through anisotropy. J Opt Soc Am 2007;24:42–50.
[23] Ding Y, Xue H, Ahmad R, Chang T, Ting ST, Simonetti OP. Paradoxical effect of the signal-to-noise ratio of GRAPPA calibration lines: a quantitative study. Med Reson Med 2015;74:231–9.
[24] Questions and answers in MRI: Gibbs (truncation) artifact, http://mriquestions.com/gibbs-artifact.html.
[25] Vovk U, Pernus F, Likar B. A review of methods for correction of intensity inhomogeneity in MRI. IEEE Trans Med Imaging 2007;26(3):405–19. https://doi.org/10.1109/TMI.2006.891486.
[26] Huang Y, Benesty J. Adaptive multi-channel least mean square and Newton algorithms for blind channel identification. Signal Process 2002;82:1127–38. https://doi.org/10.1016/S0165-1684(02)00247-5.
[27] McKenzie CA, Yeh EN, Ohliger MA, Price MD, Sodickson DK. Self-calibrating parallel imaging with automatic coil sensitivity extraction. Magn Reson Med 2002;47(3):529–38. https://doi.org/10.1002/mrm.10087.
[28] Zhao X, Robert W, Prost ZL, Li S-J. Reduction of artifacts by optimization of the sensitivity map in sensitivity-encoded spectroscopic imaging. Magn Reson Med 2005:30–4. https://doi.org/10.1002/mrm.20325.
[29] Mahesh R, Gupta R, Kalyanaraman S, Rao V, Kaliprasad P, Reddy K. Truncation artifact reduction in MRI with a new class of filters. Proceedings of the International Society for Magnetic Resonance in Medicine (ISMRM), 7th Scientific Meeting. 178. 1999http://cds.ismrm.org/ismrm-1999/PDF1/178.pdf.
[30] Hasan MK. Damped variable step-size multichannel Wiener LMS algorithm for blind channel identification with noise. Proc. CSNDSP. 2006. p. 374–7.
[31] Haque MA, Hasan MK. Variable step-size multichannel frequency-domain LMS algorithm for blind identification of finite impulse response systems. IET Signal Process 2007;1(4):182–9.
[32] Haque MA, Islam T, Hasan MK. Robust speech dereverberation based on blind adaptive estimation of acoustic channels. IEEE Trans Audio Speech Lang Process 2011;19(4):775–87.
[33] Chun IY, Adcock B, Talavage TM. Efficient Compressed Sensing SENSE pMRI reconstruction with joint sparsity promotion. IEEE Trans Med Imaging 2016;35(1):354–68.
[34] Lin F, Chen Y, Belliveau JW, Wald LL. A wavelet-based approximation of surface coil sensitivity profiles for correction of image intensity inhomogeneity and parallel imaging reconstruction. Hum Brain Mapp 2003;19(2):96–111.
[35] Aja-Fernandez S. Parallel Imaging Toolbox. www.lpi.tel.uva.es/{\~}santi; 2012. Feb.
[36] BrainWeb: Simulated Brain Database, http://brainweb.bic.mni.mcgill.ca/brainweb/.
[37] Ji JX, Son JB, Rane S. PULSAR: a MATLAB toolbox for parallel magnetic resonance imaging using array coils and multiple channel receivers. Concepts Magn Reson Part B: Magn Reson Eng 2007;31B. https://doi.org/10.1002/cmr.b.20081. 54–6124-36.
[38] Computational Biomedical Imaging Laboratory, https://www.acsu.buffalo.edu/~leiying/cbil/index_files/software.htm.
[39] Chunming Li CD, Gore John C. Multiplicative intrinsic component optimization (MICO) for MRI bias field estimation and tissue segmentation. Magn Reson Imaging 2014;32(7):913–23.
[40] Gaubitch ND, Hasan MK, Naylor P. Generalized optimal step-size for blind multichannel LMS system identification. IEEE Signal Process Lett 2006;13(10):624–7.
[41] Signal-to-noise ratio (imaging), https://en.wikipedia.org/wiki/Signal-to-noise_ratio_(imaging).
[42] Adhikari SK, Sing JK, Basu DK, Nasipuri M, Saha PK. A nonparametric method for intensity inhomogeneity correction in MRI brain images by fusion of Gaussian surfaces. Signal, image and video processing: SIViP 2014.
[43] K-Space Tool: Random Noise, http://www.revisemri.com/tools/kspace/k_noise.
[44] Li C, MRI segmentation and bias field correction https://www.mathworks.com/matlabcentral/fileexchange/.